



## Photothermal-enhanced ROS storm by hyaluronic acid-conjugated nanocatalysts to amplify tumor-specific photo-chemodynamic therapy and immune response

Tzu-Chen Lin<sup>a</sup>, I-Ju Liu<sup>a</sup>, Hsiang-Yun Chih<sup>a</sup>, Bor-Show Tzang<sup>b,c,d,e</sup>, Ju-An Liang<sup>b</sup>, Chia-Wei Kuo<sup>b</sup>, Chun-Yu Hung<sup>f</sup>, Tsai-Ching Hsu<sup>b,d,e,\*</sup>, Wen-Hsuan Chiang<sup>a,g,\*\*</sup>

<sup>a</sup> Department of Chemical Engineering, National Chung Hsing University, Taichung 402, Taiwan

<sup>b</sup> Institute of Medicine, Chung Shan Medical University, Taichung 402, Taiwan

<sup>c</sup> Department of Biochemistry, School of Medicine, Chung Shan Medical University, Taichung 402, Taiwan

<sup>d</sup> Immunology Research Center, Chung Shan Medical University, Taichung 402, Taiwan

<sup>e</sup> Department of Clinical Laboratory, Chung Shan Medical University Hospital, Taichung 402, Taiwan

<sup>f</sup> Department of Orthopedic Surgery, Jen-Ai Hospital, Taichung 402, Taiwan

<sup>g</sup> i-Center for Advanced Science and Technology (iCAST), National Chung Hsing University, Taichung 402, Taiwan

### ARTICLE INFO

#### Keywords:

Hyaluronic acid  
Photothermal nanocatalyst  
Photo-chemodynamic therapy

### ABSTRACT

Integrating photodynamic therapy (PDT) and chemodynamic therapy (CDT) shows promising potential in tumor treatment. Nevertheless, the lack of specific tumor targeting, serious photobleaching, and poor photothermal effect of photosensitizers, the intracellular low Fenton reaction efficiency, and glutathione (GSH)-elicited reactive oxygen species (ROS) depletion profoundly restrict ROS-mediated cancer therapy. To enhance ROS generation with the assistance of photothermal therapy (PTT), the hyaluronic acid (HA)-decorated Fe-MIL-88B (MIL) nanocatalysts were fabricated for tumor-targeted delivery of photosensitizer IR820. The IR820@HA-coated MIL (IHM) nanocatalysts remarkably enhanced the photothermal conversion efficacy and singlet oxygen ( $^1\text{O}_2$ ) production of IR820 and lowered IR820 photobleaching. The IHM nanocatalysts promoted the conversion of  $\text{H}_2\text{O}_2$  into toxic  $\cdot\text{OH}$  upon thermo/acidity-enhanced  $\text{Fe}^{3+}$ -mediated Fenton reaction and consumed GSH via  $\text{Fe}^{3+}$ -elicited GSH oxidation. After being internalized by 4 T1 cancer cells via CD44-mediated endocytosis, the IHM nanocatalysts under irradiation of near-infrared (NIR) laser prominently produced hyperthermia and strong ROS storm, thereby causing apoptosis and ferroptosis via mitochondria damage and lipid peroxidation, and inducing immunogenic cell death (ICD). Through HA-mediated tumor targeting, the IHM nanocatalysts effectively accumulated in 4 T1 tumor and inhibited tumor growth and lung metastasis by PTT-enhanced PDT/CDT combined with ferroptosis and ICD-amplified antitumor immune response, showing great promise in future tumor treatment.

### 1. Introduction

Cancer is an attended global health issue whose incidence continuously increases [1–3]. In the past decade, various therapeutic strategies such as surgical, chemotherapy, radiotherapy, photodynamic therapy (PDT), chemodynamic therapy (CDT), photothermal therapy (PTT), and immunotherapy have been considerably employed for cancer treatment [3–9]. Among them, PDT has emerged as a promising cancer treatment modality because of its high spatiotemporal selectivity, minimizing

invasiveness, and low adverse effects [5,9]. During PDT, the nontoxic photosensitizers are delivered to tumor sites, and the tumor regions are irradiated by specific wavelengths of light. The activated photosensitizers can convert tissue oxygen ( $\text{O}_2$ ) to toxic singlet oxygen ( $^1\text{O}_2$ ), a kind of reactive oxygen species (ROS), thus leading to oxidative injury of nucleic acids, proteins, and cell membranes to elicit cell death. However, several obstacles to photosensitizers, including the lack of specific tumor targeting, poor water solubility, and low photostability, largely limit the clinical use of PDT [9–14]. To promote the anticancer potency of PDT by

\* Correspondence to: T.-C. Hsu, Institute of Medicine, Chung Shan Medical University, Taichung 402, Taiwan.

\*\* Correspondence to: W.-H. Chiang, Department of Chemical Engineering, National Chung Hsing University, Taichung 402, Taiwan.

E-mail addresses: [htc@csmu.edu.tw](mailto:htc@csmu.edu.tw) (T.-C. Hsu), [whchiang@dragon.nchu.edu.tw](mailto:whchiang@dragon.nchu.edu.tw) (W.-H. Chiang).

<https://doi.org/10.1016/j.ijbiomac.2025.142975>

Received 9 February 2025; Received in revised form 28 March 2025; Accepted 7 April 2025

Available online 8 April 2025

0141-8130/© 2025 Elsevier B.V. All rights are reserved, including those for text and data mining, AI training, and similar technologies.

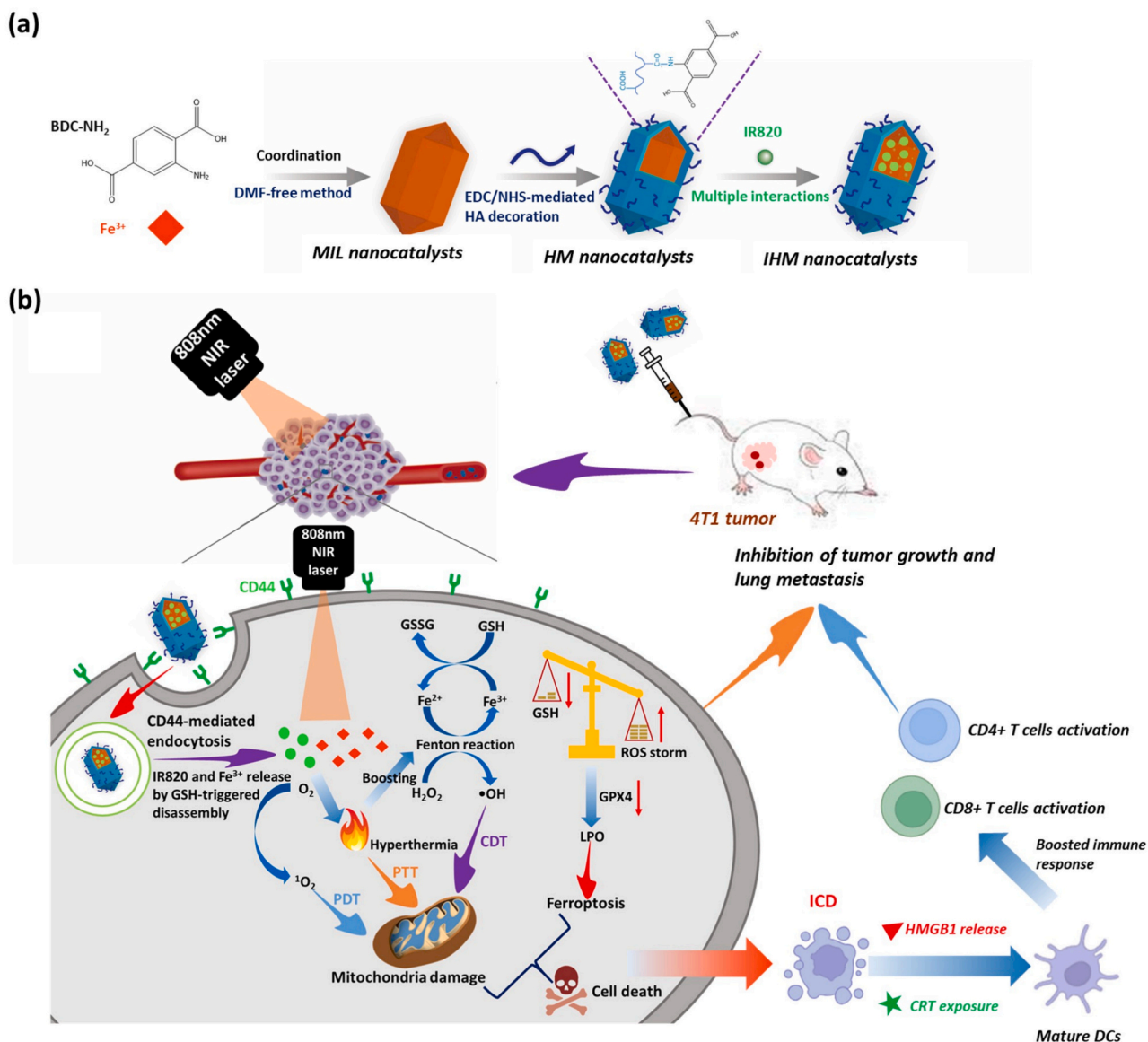
overcoming these hurdles, various nanovehicles (e.g., polymeric micelles, liposomes, organic or inorganic nanoparticles, etc.) have been fabricated to achieve tumor-targeted photosensitizer delivery [9–14]. Distinct from oxygen-consuming PDT, CDT utilizes transition metal ions (e.g.,  $\text{Fe}^{2+/3+}$ ,  $\text{Ce}^{3+/4+}$ ,  $\text{Cu}^{1+/2+}$ ,  $\text{Mn}^{2+/4+}$ , etc.) to transform intracellular  $\text{H}_2\text{O}_2$  into a cytotoxic hydroxyl radical ( $\bullet\text{OH}$ ) upon Fenton reaction, thus provoking oxidative damage of cancer cells. Compared to  $^1\text{O}_2$ ,  $\bullet\text{OH}$ , the most toxic ROS, leads to mitochondria damage and lipid peroxidation (LPO), which is beneficial for ROS-mediated ferroptosis [15–17]. Unfortunately, due to the limited  $\text{H}_2\text{O}_2$  concentration and low catalytic efficiency of the Fenton reaction in vivo, CDT displayed restricted anticancer effects in previous works [3,16–18]. Besides, glutathione (GSH), a major intracellular antioxidant overexpressed in cancer cells, potentially exhausts ROS to keep intracellular homeostasis, thereby preventing cells from PDT/CDT-elicited oxidative harm [18–20].

Considering that a single ROS-mediated treatment cannot effectively suppress tumor growth, the combination of PDT and CDT has emerged promising for simultaneously generating toxic  $^1\text{O}_2$  and  $\bullet\text{OH}$  in cancer cells to boost anticancer effects upon increased intracellular ROS levels [15,21–24]. Although various functionalized nanoparticles have been developed for PDT/CDT combination therapy, the enhancement of antitumor efficacy is still not satisfied. Increased studies reported that the hyperthermia of tumor sites by PTT augmented intratumoral blood flow and oxygenation, which is beneficial for PDT [25,26], and accelerates metal ions-mediated Fenton reaction to enhance toxic  $\bullet\text{OH}$  production for improved CDT [27–29]. For example, Shen's group fabricated a polydopamine-coated  $\text{Fe}^{3+}$ -rich metal-organic framework (MOF) nanoparticle to co-deliver the chemical drug piperlongumine and photosensitizer IR820 [17]. Through CDT and PTT combination, the therapeutic nanoparticles effectively elicited ferroptosis, pyroptosis, and immune response to inhibit tumor growth. Furthermore, heat stress can affect intracellular inherent resistance, such as increasing the depletion of GSH, which assists ROS generation. As a noninvasive therapeutic method, PTT has been demonstrated to elicit rapid necrosis, thus promoting local immunogenic cell death (ICD) and provoking damage-associated molecular patterns (DAMPs), such as secreted adenosine triphosphate (ATP), exposed calreticulin (CRT), and liberated high mobility group protein B1 (HMGB1) to boost tumor immunogenicity [7,30–32]. Therefore, integrating PTT with PDT/CDT combination therapy is highly desirable to realize photothermal-boosted ROS storm and GSH consumption for better antitumor efficacy. For example, Liu's group fabricated L-buthionine-sulfoximine (BSO) modified  $\text{FeS}_2$  nanoparticles (BSO- $\text{FeS}_2$  NPs) for photoacoustic imaging-guided PTT/CDT/PDT combination cancer therapy [33]. The  $\text{FeS}_2$  nanoparticles exhibited high photothermal conversion efficiency and promoted ROS generation via photothermal-improved Fenton reaction and photocatalytic ability. Furthermore, BSO- $\text{FeS}_2$  NPs efficiently depleted GSH and accelerated the accumulation of ROS, thus amplifying the PDT/CDT-mediated antitumor efficacy. Also, BSO- $\text{FeS}_2$  NPs activated the repolarization of macrophages from M2 to M1 to elicit potential tumor immunotherapy. Moreover, to achieve a second near-infrared window (NIR-II)-triggered PTT and PDT combined with CDT, the gold nanopyramid@copper sulfide coated with red cell membrane as the nanotheranostic was developed by Chen et al. [34]. The multifunctional nanoplateforms remarkably suppressed tumor growth and elicited DAMP, such as ATP, CRT, and HMGB1, in dying cells based on the NIR-II photo/chemodynamic therapy, thus simultaneously triggering adaptive antitumor immune responses. Despite the remarkable progress in developing photothermal nanoparticles capable of merging PDT and CDT to boost immune response for tumor treatment, the fabrication of these nanoparticles often involves the utilizing of non-biocompatible and complicated materials, toxic organic solvents, multiple-step or harsh synthetic approaches, thus not beneficial to clinical application.

Recently, nano-sized metal-organic frameworks (nMOFs), consisting of inorganic metal ions and organic bridging ligands, have become a

promising biomaterial due to good biocompatibility, designed size and stimulus responsiveness, delivery and controlled release of drug payloads [35]. Among these nMOFs, iron-based nMOFs (e.g., MIL-53, MIL-88B, MIL-100, MIL-101, etc.) used as nanocatalysts for ROS-mediated cancer treatment have received much attention due to their high porosity, nontoxic nature, biodegradability, and tumor microenvironment-responsiveness [36–38]. However, most of these iron-based nMOFs were prepared using a harsh hydrothermal method involving high reaction temperature and pressure [36,37] and the use of dimethylformamide (DMF), a category 2 A carcinogen by the International Agency for Research on Cancer, as the reaction solvent. The DMF-involved hydrothermal method will largely limit the clinical translation of the above iron-based nMOFs. IR820, an analog of indocyanine green, is an anionic amphiphilic photosensitizer that produces hyperthermia and toxic  $^1\text{O}_2$  under an 808 nm NIR laser irradiation for PTT and PDT [39–41]. However, IR820, with a short lifetime in vivo ( $t_{1/2} = 185$  min), is easily metabolized by the liver, leading to reduced accumulation at the tumor sites, which is not good for cancer therapy [40]. Hyaluronic acid (HA), a natural polysaccharide composed of a simple repeating disaccharide of d-glucuronic acid and N-acetyl-d-glucosamine linked by  $\beta(1 \rightarrow 3)$  linkages, is widely utilized as biomaterials due to its high biocompatibility, water solubility, immunogenicity, and hydrophilicity, and several reactive sites for chemical modification [8,11,16]. Also, HA has been decorated on the surfaces of various nanocarriers for tumor-targeted drug delivery because HA can specifically bind to the CD44 receptors overexpressed on numerous cancer cell membranes. The HA-modified nanoparticles can be efficiently internalized into tumor tissues by receptor-mediated endocytosis [8,11,16].

Inspired by the aforementioned studies, to effectively inhibit tumor growth and metastasis by the PTT-enhanced photo-chemodynamic therapy combined with the antitumor immune response, we herein adopted the DMF-free and mild method instead of the traditional hydrothermal method to fabricate the tumor-targeting  $\text{Fe}^{3+}$ -rich MIL-88B (MIL) nanocatalysts as IR820 vehicles (Scheme 1). Through the coordination between  $\text{FeCl}_3$  molecules and BDC- $\text{NH}_2$  ligands, the MIL nanocatalysts were attained and covalently decorated with HA segments for specific CD44 targeting. Afterward, IR820 molecules were efficiently encapsulated into HA-MIL (HM) nanocatalysts by multiple  $\pi$ - $\pi$  stacking, hydrophobic, and coordination interactions. The resulting IR820-encapsulated HM (IHM) nanocatalysts were characterized to exhibit a spindle-like shape, high IR820 payloads (ca 19.1 wt%), prominent colloidal stability, and enhanced photothermal conversion efficiency and stability of IR820. The IHM nanocatalysts were remarkably disintegrated under GSH-rich and weakly acidic conditions, thus promoting  $\text{Fe}^{3+}$  and IR820 release. Notably, the IHM nanocatalysts generated  $\text{Fe}^{2+}$  by depleting GSH and displayed thermo/acidity-boosted  $\text{Fe}^{3+}$ -mediated Fenton reaction, thereby promoting the conversion of  $\text{H}_2\text{O}_2$  into  $\bullet\text{OH}$ . After being internalized by CD44-overexpressed 4 T1 mouse breast cancer cells upon CD44-mediated endocytosis, the IHM nanocatalysts exposed to irradiation of 808 nm NIR laser remarkably consumed intracellular GSH and produced hyperthermia and strong ROS storm composed of  $\bullet\text{OH}$  and  $^1\text{O}_2$ , thus efficiently eliciting apoptosis and ferroptosis via mitochondria damage and LPO, and inducing ICD to liberate CRT and HMGB1. Through HA-mediated tumor targeting, the IHM nanocatalysts effectively accumulated in 4 T1 tumor and effectively suppressed tumor growth and lung metastasis by the NIR-triggered hyperthermia and ROS storm combined with ICD-amplified immune response (Scheme 1b). To the best of our knowledge, this work is the first report to develop tumor-targeting IHM nanocatalysts capable of effectively inhibiting tumor growth and lung metastasis by PTT-enhanced PDT/CDT and ferroptosis combined with boosted antitumor immune response, thus showing great promise in future tumor treatment.



**Scheme 1.** Schematic illustration of the fabrication approaches of IHM nanocatalysts and their antitumor potency by PTT-enhanced PDT/CDT and ferroptosis combined with antitumor immune response.

## 2. Materials and methods

### 2.1. Materials

Iron (III) chloride ( $\text{FeCl}_3$ ) was purchased from SHOWA. Hyaluronic acid sodium salt (HA) ( $\geq 91\%$ , MW = 3000–5000 Da) was obtained from Glentham Life Science Ltd. N-(3-dimethylaminopropyl)-N'-ethylcarbodiimide hydrochloride (EDC) was obtained from Matrix Scientific. N-hydroxysuccinimide (NHS) was purchased from Alfa Aesar. 2-aminoterephthalic acid ( $\text{BDC-NH}_2$ ), IR820, propidium iodide (PI), 2',7'-dichlorodihydrofluorescein diacetate (DCFH-DA), 3-(4,5-Dimethylthiazol-2-yl)-2,5-diphenyltetrazolium bromide (MTT), 1,3-diphenylisobenzofuran (DPBF), and dulbecco's modified Eagle medium (DMEM) were obtained from Sigma-Aldrich (USA). 1,10-phenanthroline monohydrate (Phe,  $\geq 99.5\%$ ) was attained from Thermo Fisher Scientific. 2,2'-azino-bis(3-ethylbenzothiazoline-6-sulfonic acid) (ABTS, 95%) was obtained from Combi-Blocks (USA). 5,5'-dithiobis(2-nitrobenzoic acid) (DTNB, 99%) was purchased from Fluorochem (UK). 3,3',5,5'-Tetramethylbenzidine (TMB, 99%) was purchased from Acros Organics (USA). Calcein AM was purchased from AAT Bioquest. JC-1 and

RhoNox-1 were obtained from MedChemExpress. Hoechst 33342 and BIDOPY<sup>581/591</sup> were purchased from Invitrogen. Anti-CRT antibodies and anti-HMGB1 antibodies were purchased from GeneTex. AlexaFluo 488® AffiniPure Goat Anti-Rabbit IgG(H + L) was attained from Jackson ImmunoResearch. Ki67 antibodies (no. ab15580) and anti-glutathione peroxidase 4 (GPX4) antibodies (no. ab125066) were obtained from Abcam. All other chemicals were used as received. Tramp-C1 (murine colon adenocarcinoma cell line) and 4 T1 (murine mammary carcinoma cell line) were acquired from Food Industry Research and Development Institute (Hsinchu City, Taiwan).

### 2.2. Preparation of MIL nanocatalysts

$\text{FeCl}_3$  (8.9 mg) and  $\text{BDC-NH}_2$  (20 mg) were dissolved in ethanol (5 mL, 95%) respectively.  $\text{BDC-NH}_2$  solution was added to the  $\text{FeCl}_3$  solution and stirred at 40 °C for 1.5 h. MIL nanocatalysts were collected by centrifugation (16,000 rpm, 20 min) and washed with ethanol and deionized water. The as-prepared MIL nanocatalysts were dispersed in deionized water and stored at 4 °C for further use.

### 2.3. Preparation of HM nanocatalysts

HA (2 mg), EDC (5 mg), and NHS (5 mg) were dissolved in deionized water (1 mL) and further stirred at room temperature for 30 min to activate the carboxyl group of HA. MIL nanocatalysts solution (1 mL, 1 mg/mL) was dropwise added to the activated HA solution and stirred for 24 h. HM nanocatalysts were collected by centrifugation (16,000 rpm, 20 min) and washed triplicate with deionized water. The as-prepared HM nanocatalysts were dispersed in deionized water and stored at 4 °C for further use.

### 2.4. Preparation of IHM nanocatalysts

HA (2 mg), EDC (5 mg), and NHS (5 mg) were dissolved in deionized water (1 mL) and further stirred at room temperature for 30 min to activate the carboxyl group of HA. MIL nanocatalysts solution (1 mL, 1 mg/mL) was dropped slowly into the activated HA solution and stirred for 24 h. IR820 solution (0.5 mL, 0.5 mg/mL) was dropwise added to the above solution and stirred for 24 h. IHM nanocatalysts were purified and collected by centrifugation (16,000 rpm, 20 min) and washed triplicate with deionized water to remove unloaded IR820. The as-prepared IHM nanocatalysts were dispersed in deionized water and stored at 4 °C for

$$\text{Loading content of IR820 (wt\%)} = \frac{\text{Weight of IR820 in feed} - \text{weight of IR820 in the supernatant}}{\text{Total weight of IHM nanocatalysts}} \times 100\%$$

further use.

### 2.5. Characterization

A D8 Discover X-ray diffractometer (Bruker, Germany) with CuK $\alpha$  radiation (40 kV,  $\lambda = 0.15$  nm) was utilized to obtain the X-ray diffraction (XRD) patterns of MIL, HM, and IHM nanocatalysts. The morphology of various nanocatalysts was observed by transmission electron microscope (TEM) (JEM-1400 FLASH, JEOL, Japan) and scanning electron microscope (SEM) (JEOL JSM-7800F Prime Schottky Field Emission SEM, Japan). X-ray energy dispersive spectroscopy (EDS) elemental mapping of IHM nanocatalysts was acquired with TEM (JEM-F200, JEOL). The particle size and size distribution of various nanocatalysts dispersed in aqueous solutions at pH 7.4 or 5.0 were determined by dynamic light scattering (DLS) using a Brookhaven BI-200SM goniometer equipped with a BI-9000 AT digital correlator using a solid-state laser (35 mW,  $\lambda = 637$  nm) detected at a scattering angle of 90°. The colloidal stability of IHM nanocatalysts dispersed in 0.9 % saline solution, 10 % FBS-containing saline solution, and 10 % FBS-containing DMEM, respectively, at 37 °C, was evaluated by the Brookhaven BI-200SM goniometer. The zeta potential of MIL, HM, and IHM nanocatalysts dispersed in 0.01 M NaCl aqueous solutions was measured with a Litesizer 500 (Anton Paar, USA). At least triplicate measurements of each sample were conducted and then averaged. The absorption spectra of IR820 molecules, HM, and IHM nanocatalysts in 0.9 % saline solution were obtained using a UV/Vis spectrophotometer (U2900, Hitachi, Japan). The chemical compositions of various nanocatalysts, HA segments, and BDC-NH $_2$  molecules were characterized by Fourier transform infrared (FT-IR) microscopy (FT-720, HORIBA, Japan). X-ray photoelectron spectroscopy (XPS) analysis of IHM nanocatalysts was performed by a PHI 5000 VersaProbe III X-ray photoelectron spectrometer (ULVAC-PHI, Japan) with AlK $\alpha$  radiation ( $h\nu = 1486.6$  eV) at 15 kV and 150 W.

### 2.6. Determination of Fe<sup>3+</sup> and IR820 content

IHM nanocatalysts solution (0.25 mL, 40  $\mu$ g/mL) was mixed with vitamin C (0.25 mL, 40 mM) and Phe (0.5 mL, 2 mg/mL) and then reacted for 30 min at room temperature. The absorbance of the resulting solution at 509 nm was analyzed by a UV/Vis spectrophotometer. The calibration curve for Fe<sup>3+</sup> loading characterization was established by absorbance of Fe<sup>3+</sup> with various concentrations in vitamin C/Phe-containing solution (Fig. S1). The Fe<sup>3+</sup> loading content of IHM nanocatalysts was calculated using the following formula:

$$\text{Loading content of Fe}^{3+} \text{ (wt\%)} = \frac{\text{Weight of Fe}^{3+} \text{ loaded}}{\text{Total weight of IHM nanocatalysts}} \times 100\%$$

The IR820 loading content of IHM nanocatalysts was determined as follows. The IHM nanocatalyst solution was centrifuged (16,000 rpm, 20 min) to collect the supernatant, and the absorbance of IR820 in the supernatant at 818 nm was measured by a UV/Vis spectrophotometer. The calibration curve for IR820 loading characterization was established by absorbance of IR820 with various concentrations in ethanol/deionized water (1/4) solution (Fig. S2). The loading content (LC) of IR820 was calculated by the following formula:

### 2.7. Photothermal conversion efficiency ( $\eta$ ) of IR820 and IHM nanocatalysts

Free IR820 molecules, HM nanocatalysts, and IHM nanocatalysts dispersed in 1.0 mL 0.9 % saline (IR820 concentration = 11.8  $\mu$ g/mL, Fe<sup>3+</sup> concentration = 17.6  $\mu$ g/mL), respectively, were irradiated by 808 nm NIR laser (1.0 W/cm<sup>2</sup>) for 5 min. The solution temperatures and infrared thermographic maps were recorded with an infrared thermal imaging camera (Thermo Shot F20, NEC Avio Infrared Technologies, Germany). Also, according to the data from the cooling status, the photothermal conversion efficiency ( $\eta$ ) of the free IR820 molecules and IHM nanocatalysts was calculated using the formula presented in the Supporting Information. Moreover, the temperature elevation of an aqueous solution containing IHM nanocatalysts of different concentrations exposed to laser irradiation (1.0 W/cm<sup>2</sup>) for 5 min was determined by the above apparatus. On the other hand, to assess the photothermal stability, an aqueous solution containing free IR820 molecules or IHM nanocatalysts (IR820 concentration = 16.5  $\mu$ g/mL) was irradiated with 808 nm laser (1.0 W/cm<sup>2</sup>) for 5-min laser on and 5-min laser off cycles. Furthermore, the IR820 absorbance of free IR820 molecule and IHM nanocatalyst solutions receiving various on/off cycles of laser irradiation was determined by UV/Vis spectrophotometer. On the other hand, the temperature change of IHM nanocatalysts of 50  $\mu$ g/mL under NIR laser irradiation of different power densities was monitored by an infrared thermal imaging camera.

### 2.8. GSH-depleting and Fe<sup>2+</sup>-generating ability of IHM nanocatalysts

The GSH depletion capability of IHM nanocatalysts was studied using a DTNB assay. IHM nanocatalysts solution (0.9 mL, 222  $\mu$ g/mL) was mixed with GSH solution (0.1 mL, 4 mM) and incubated at 37 °C for 1, 3, 6, and 24 h. Afterward, the mixture was centrifuged (16,000 rpm, 20 min) to collect the supernatant. The supernatant (0.5 mL) was added

to DTNB solution (0.5 mL, 0.2 mM) and further reacted for 30 min. Finally, the UV/Vis spectrum of the resulting solution was obtained by UV/Vis spectrophotometer.

The Phe assay was utilized to confirm that  $\text{Fe}^{3+}$  ions of IHM nanocatalysts can be reduced to  $\text{Fe}^{2+}$  ions by GSH. Briefly, IHM nanocatalysts (50  $\mu\text{g}/\text{mL}$ ) were treated with GSH (0.4 mM) and Phe (0.1 mg/mL) at 37 °C for 1 h, followed by centrifugation (16,000 rpm, 20 min) to collect the supernatant. The absorption spectrum of the supernatant was attained by a UV/Vis spectrophotometer.

## 2.9. GSH-responsive disassembly of IHM nanocatalysts

IHM nanocatalysts were dispersed in aqueous solutions of pH 7.4 or 5.0 with or without GSH (10 mM) and incubated at 37 °C. At a predetermined time, the particle size of IHM nanocatalysts was determined by a Brookhaven BI-200SM goniometer. Furthermore, the morphology of IHM nanocatalysts treated with the above conditions for 6 h was observed by TEM.

## 2.10. In vitro $\text{Fe}^{3+}$ and IR820 release

IHM nanocatalysts dispersion (0.5 mL) was dialyzed (Cellu Sep MWCO 12000–14,000) against pH 7.4 tris buffer and pH 5.0 acetate buffer with or without 10 mM GSH (25 mL), respectively, at 37 °C. The dialysate (0.25 mL) was taken out at the prescribed time and replaced with an equivalent volume of fresh buffer. The dialysate was mixed with vitamin C (0.25 mL, 40 mM) and Phe (0.5 mL, 2 mg/mL) for 30 min. The absorbance of the resulting solution at 509 nm was analyzed by UV/Vis spectrophotometer to attain the amount of  $\text{Fe}^{3+}$  liberated from IHM nanocatalysts.

For IR820 release, IHM nanocatalysts were dispersed in pH 7.4 tris buffer and pH 5.0 acetate buffer with or without 10 mM GSH, respectively, at 37 °C. A minor 10 v/v% DMSO was added to the above solutions to avoid precipitation of the hydrophobic IR820 molecules released from IHM nanocatalysts, being beneficial for analysis. At the predetermined time, the dispersion was centrifuged (16,000 rpm, 20 min). The absorbance of the supernatant at 818 nm was measured by UV/Vis spectrophotometer to obtain the amount of IR820 liberated from IHM nanocatalysts.

## 2.11. Catalytic performance of nanocatalysts

The catalytic capability ( $\bullet\text{OH}$  production) of IHM nanocatalysts was evaluated by determining the absorption of oxTMB produced from the oxidation of TMB by  $\bullet\text{OH}$ . IHM nanocatalysts (50  $\mu\text{g}/\text{mL}$ ) were dispersed in aqueous solutions of pH 7.4, 6.0, and 5.0 containing 100  $\mu\text{M}$   $\text{H}_2\text{O}_2$  and 0.5 mM TMB and then incubated in the dark at 37 °C for 10 min. The above solutions were centrifuged (16,000 rpm, 10 min) to collect the supernatant. The UV/Vis spectrum of the supernatant was obtained with a UV/Vis spectrophotometer. Also, the ABTS assay was utilized to assess the  $\bullet\text{OH}$  generation of IHM nanocatalysts. IHM nanocatalysts (50  $\mu\text{g}/\text{mL}$ ) in aqueous solutions of pH 7.4, 6.0, and 5.0 containing 100  $\mu\text{M}$   $\text{H}_2\text{O}_2$  and 0.5 mM ABTS were incubated in the dark at 25, 37, or 50 °C for 1 h. The above solutions were centrifuged (16,000 rpm, 10 min) to collect the supernatant. The UV/Vis spectrum of the supernatant was acquired by a UV/Vis spectrophotometer.

## 2.12. $^1\text{O}_2$ generation

IR820 molecule and IHM nanocatalyst (IR820 concentration = 11.8  $\mu\text{g}/\text{mL}$ ) solution were irradiated with 808 nm NIR laser in the presence of DPBF (50  $\mu\text{g}/\text{mL}$ ) for 1, 5, and 10 min. After that, the DPBF fluorescence signals of the mixture in the range 420–650 nm were determined with a fluorescence spectrometer (F-2700, Hitachi, Japan).

## 2.13. In vitro cellular uptake

4 T1 cells seeded onto 22 mm round glass coverslips in 6-well plates ( $2.0 \times 10^5$  cells/well) were incubated at 37 °C for 24 h. Cells were treated with IR820 molecules or IHM nanocatalysts (IR820 concentration = 2.95  $\mu\text{g}/\text{mL}$ ) in the presence of  $\text{H}_2\text{O}_2$  (100  $\mu\text{M}$ ) at 37 °C for 1 h and 4 h. After being washed twice with Hanks' balanced salt solution (HBSS), the cells were fixed with paraformaldehyde (4 %) and stained with Hoechst 33342. The cellular images were attained with a confocal laser scanning microscope (CLSM) (Olympus, FluoView FV3000, Japan) at 405 and 782 nm excitation wavelengths for Hoechst and IR820, respectively. Moreover, the average IR820 fluorescence intensity of 4 T1 cells receiving different treatments was analyzed by Image J ( $n = 10$ ). On the other hand, 4 T1 cells ( $2 \times 10^5$  cells/well) seeded in 6-well plates were incubated with free IR820 molecules or IHM nanocatalysts (IR820 concentration = 2.95  $\mu\text{g}/\text{mL}$ ) with or without free HA segments (10 mg/mL) for 4 h at 37 °C. After being detached with trypsin-EDTA solution, the IR820 fluorescence signals of the treated 4 T1 cells suspended in PBS (1.0 mL) were measured by the FACSCalibur flow cytometer (BD Bioscience).

## 2.14. Intracellular $\text{Fe}^{2+}$ and GSH level

4 T1 cells seeded onto 22 mm round glass coverslips in 6-well plates ( $1.0 \times 10^5$  cells/well) were incubated at 37 °C for 24 h. Cells were then treated with IR820, HM, or IHM nanocatalysts (IR820 concentration = 11.8  $\mu\text{g}/\text{mL}$ ,  $\text{Fe}^{3+}$  concentration = 17.6  $\mu\text{g}/\text{mL}$ ) in the presence of  $\text{H}_2\text{O}_2$  (100  $\mu\text{M}$ ) for 24 h. To analyze the intracellular  $\text{Fe}^{2+}$  level, the cells were incubated with RhoNox-1 (5  $\mu\text{M}$ ) at 37 °C for 30 min. The intracellular RhoNox-1 fluorescence was observed by fluorescence microscopy (ZEISS Axio Imager M2) at an excitation wavelength of 540 nm.

4 T1 cells were seeded in 6-well plates ( $1.0 \times 10^5$  cells/well) and incubated at 37 °C for 24 h. Cells were treated with HM or IHM nanocatalysts (IR820 concentration = 11.8  $\mu\text{g}/\text{mL}$ ,  $\text{Fe}^{3+}$  concentration = 17.6  $\mu\text{g}/\text{mL}$ ) in the presence of  $\text{H}_2\text{O}_2$  (100  $\mu\text{M}$ ) for 24 h. After washed twice with PBS, cells were detached with trypsin-EDTA and collected by centrifugation (1500 rpm, 5.5 min). The cells were irradiated with 808 nm NIR laser (1.0 W/cm<sup>2</sup>, 5 min) and further dispersed in 0.3 mL RIPA lysis buffer, followed by freezing and thawing for cell lysis. Subsequently, the lysate was centrifuged (10,000 rpm, 10 min) to remove the impurities. To determine the intracellular GSH level, the supernatant (0.1 mL) was mixed with DTNB solution (0.05 mL, 1 mM) and analyzed by a Biotek 800TS microplate reader at 405 nm. Moreover, the treated cells without NIR laser irradiation were used for comparison.

## 2.15. Intracellular ROS level

4 T1 cells seeded onto 22 mm round glass coverslips in 6-well plates ( $1.0 \times 10^5$  cells/well) were incubated for 24 h. Cells were treated with IR820, HM, or IHM nanocatalysts (IR820 concentration = 11.8  $\mu\text{g}/\text{mL}$ ,  $\text{Fe}^{3+}$  concentration = 17.6  $\mu\text{g}/\text{mL}$ ) in the presence of  $\text{H}_2\text{O}_2$  (100  $\mu\text{M}$ ) for 24 h. After that, the cells were irradiated by 808 nm NIR laser (1.0 W/cm<sup>2</sup>, 5 min). Moreover, the treated cells without NIR laser irradiation were used for comparison. To analyze the ROS level in 4 T1 cells, the cells were treated with DCFH-DA (5  $\mu\text{M}$ ) at 37 °C for 30 min and washed with HBSS, followed by immobilization with 4 % formaldehyde. The cellular images were attained using CLSM (Olympus, FluoView FV3000, Japan) at an excitation wavelength of 485 nm for DCF.

## 2.16. Intracellular lipid peroxidation

4 T1 cells were seeded onto 22 mm round glass coverslips in 6-well plates ( $1.0 \times 10^5$  cells/well) and incubated at 37 °C for 24 h. Cells were treated with IR820, HM, or IHM nanocatalysts (IR820 concentration = 11.8  $\mu\text{g}/\text{mL}$ ,  $\text{Fe}^{3+}$  concentration = 17.6  $\mu\text{g}/\text{mL}$ ) in the presence of  $\text{H}_2\text{O}_2$  (100  $\mu\text{M}$ ) for 24 h. After that, the cells were irradiated by 808 nm NIR

laser (1.0 W/cm<sup>2</sup>, 5 min). To evaluate intracellular lipid peroxidation, the cells were incubated with BIDOPY<sup>581/591</sup> (2 μM) at 37 °C for 30 min and washed two times with HBSS, followed by immobilization with 4 % formaldehyde. The intracellular oxidized BIDOPY<sup>581/591</sup> fluorescence was observed by fluorescent microscopy (ZEISS Axio Imager M2) at an excitation wavelength of 500 nm. Furthermore, the treated cells without NIR laser irradiation were used for comparison.

### 2.17. Mitochondrial membrane potential (MMP)

4 T1 cells were seeded onto 22 mm round glass coverslips in 6-well plates (1.0 × 10<sup>5</sup> cells/well) and incubated at 37 °C for 24 h. Cells were treated with IR820, HM, or IHM nanocatalysts (IR820 concentration = 11.8 μg/mL, Fe<sup>3+</sup> concentration = 17.6 μg/mL) in the presence of H<sub>2</sub>O<sub>2</sub> (100 μM) for 24 h. After that, the cells were irradiated with 808 nm NIR laser (1.0 W/cm<sup>2</sup>, 5 min) and washed two times with HBSS, followed by immobilization with 4 % formaldehyde. The cellular images were acquired using fluorescence microscopy (ZEISS Axio Imager M2) at 485 and 535 nm excitation wavelengths for JC-1 monomer and JC-1 aggregate, respectively. Moreover, the average JC-1 green and red fluorescence intensity of 4 T1 cells receiving different treatments was analyzed by Image J (n = 10), and the ratio of JC-1 green and red fluorescence intensity was attained.

### 2.18. In vitro cytotoxicity

4 T1 cells or TRAMP-C1 cells were seeded in 6-well plates (2.0 × 10<sup>5</sup> cells/well) and incubated at 37 °C for 24 h. Cells were treated with IR820, HM, or IHM nanocatalysts of different concentrations in the presence of H<sub>2</sub>O<sub>2</sub> (100 μM) for 4 h. After being washed twice with PBS, cells were detached with Trypsin-EDTA and collected by centrifugation (1500 rpm, 5.5 min). After that, the cell pellets were dispersed in DMEM (0.1 mL) and irradiated by 808 nm NIR laser (1.0 W/cm<sup>2</sup>, 1 min). The laser-treated cells were re-seeded in 12-well plates and incubated for 24 h. After discarding the culture medium, MTT (0.25 mg/mL, 1 mL) was added to each well and incubated at 37 °C for 3 h. Subsequently, DMSO (0.8 mL) was added to dissolve the precipitates, and the absorbance of the resulting solution at 570 nm was measured by a BioTek 800TS microplate reader. The cytotoxicity of different formulations on 4 T1 cells without NIR laser irradiation was also assessed in a similar manner. For comparison, without NIR laser irradiation, the cytotoxicity of IHM nanocatalysts on the healthy WS1 cells (human skin fibroblast cells) was evaluated by the above approach.

### 2.19. Live/dead cell staining

4 T1 cells were seeded in 12-well plates (2.0 × 10<sup>5</sup> cells/well) and incubated at 37 °C for 24 h. Cells were treated with IR820, HM, or IHM nanocatalysts (IR820 concentration = 11.8 μg/mL, Fe<sup>3+</sup> concentration = 17.6 μg/mL) in the presence of H<sub>2</sub>O<sub>2</sub> (100 μM) for 4 h. Afterward, cells were exposed to 808 nm NIR laser (1.0 W/cm<sup>2</sup>, 1 min). The live cells were stained with Calcein-AM (2 μM) at 37 °C for 45 min and then stained with propidium iodide (PI, 4.5 μM) for 15 min. The cellular images were attained using NIB-100F inverted fluorescent biological microscope (Nanjing Jiangan Novel Optics Co., Ltd., China).

### 2.20. ICD induction capability

4 T1 cells were seeded onto 22 mm round glass coverslips in 6-well plates (1.0 × 10<sup>5</sup> cells/well) and incubated at 37 °C for 24 h. Cells were treated with IR820, HM, or IHM nanocatalysts (IR820 concentration = 11.8 μg/mL, Fe<sup>3+</sup> concentration = 17.6 μg/mL) in the presence of H<sub>2</sub>O<sub>2</sub> (100 μM) for 24 h. Afterward, the cells were irradiated with an 808 nm NIR laser (1.0 W/cm<sup>2</sup>, 5 min). After being fixed with paraformaldehyde (4 %) for 15 min, for CRT staining, the cells were blocked with BSA (5 %) for 1 h, while for HMGB1 staining, the cells were permeabilized with

TritonX-100 (0.1 %) for 15 min before blocking step. Subsequently, the cells were incubated with anti-CRT or anti-HMGB1 antibody at 4 °C overnight and further incubated with Alexa Fluor 488-conjugated secondary antibody at room temperature for 1 h. Finally, 4 T1 cells were stained with Hoechst 33342 and observed by CLSM at 405 and 495 nm excitation wavelengths for Hoechst and Alexa Fluor 488, respectively. Furthermore, the CRT fluorescence of 4 T1 cells receiving different treatments was quantified by Image J (n = 10).

### 2.21. Animal and tumor model

Female BALB/c mice (5 ~ 6 weeks old) were obtained from the National Laboratory Animal Center (Taiwan) and cared according to the Guidance Suggestions for the Care and Use of Laboratory Animals, approved by the Administrative Committee on Animal Research in the Chung Shan Medical University (Taiwan) (IACUC Approval No: 112040). To establish the 4 T1 tumor model, 2 × 10<sup>6</sup> 4 T1 cells in PBS (0.1 mL) were subcutaneously injected into the right thigh of mice. Tumor volume (V) was calculated as follows:  $V = L \times W^2/2$  (W: widest length of tumor, L: longest length of tumor).

### 2.22. In vivo/ex vivo fluorescence imaging

When tumor volume reached about 100 mm<sup>3</sup>, saline, IR820 molecules, or IHM nanocatalysts solution (100 μL, dosage of IR820: 1.0 mg/kg) was injected into the mice via the tail vein. At 2, 4, 6, and 24 h post-injection, the in vivo imaging of mice was obtained using IVIS (IVIS Lumina II, Caliper, Life Sciences, MA, USA). The treated mice were sacrificed at 24 h post-injection, and the major organs and tumors were collected for ex vivo fluorescence imaging by IVIS.

### 2.23. In vivo thermal imaging

When tumor volume reached about 100 mm<sup>3</sup>, saline, IR820, or IHM nanocatalysts solution (100 μL, dosage of IR820: 1.0 mg/kg) was injected into the mice via the tail vein. At 4 h post-injection, the tumor site was irradiated with 808 nm NIR laser (1.0 W/cm<sup>2</sup>, 5 min), and the temperature was measured by an infrared thermal imaging camera.

### 2.24. In vivo tumor growth inhibition

When tumor volume reached about 100 mm<sup>3</sup>, mice were randomly divided into four groups (n = 4): (i) Saline: (ii) IR820 molecules + NIR laser: (iii) IHM nanocatalysts: (iv) IHM nanocatalysts + NIR laser. Mice were intravenously injected with the above formulations (injection volume: 100 μL, dosage of IR820: 1.0 mg/kg) at day 0 and day 1. At 4 h post-injection, the tumor site was irradiated with 808 nm NIR laser (1.0 W/cm<sup>2</sup>, 5 min). The tumor volumes and body weight of mice were measured every two days. On day 14, all mice were euthanized, the tumors and main organs were harvested, and the tumor and spleen were weighed. The excised lung tissues were stained with Bouin's solution, and the number of lung metastatic nodules was recorded. The collected tumors and organs were fixed with 4 % paraformaldehyde and then processed routinely in paraffin. Next, the tumors and organs were sectioned into 4 μm thick slices for hematoxylin and eosin (H&E) staining and then observed by digital microscope.

### 2.25. Immunohistochemistry (IHC) staining and analysis

Tumor sections were formalin-fixed in paraffin and stained with primary anti-ki67, GPX4, CD4, CD8α, HMGB1, and CD86 antibodies via a typical IHC procedure. ImageJ software was used to quantify the numbers of positive cells using 3 to 5 randomly selected fields of view (FOV) per slide.

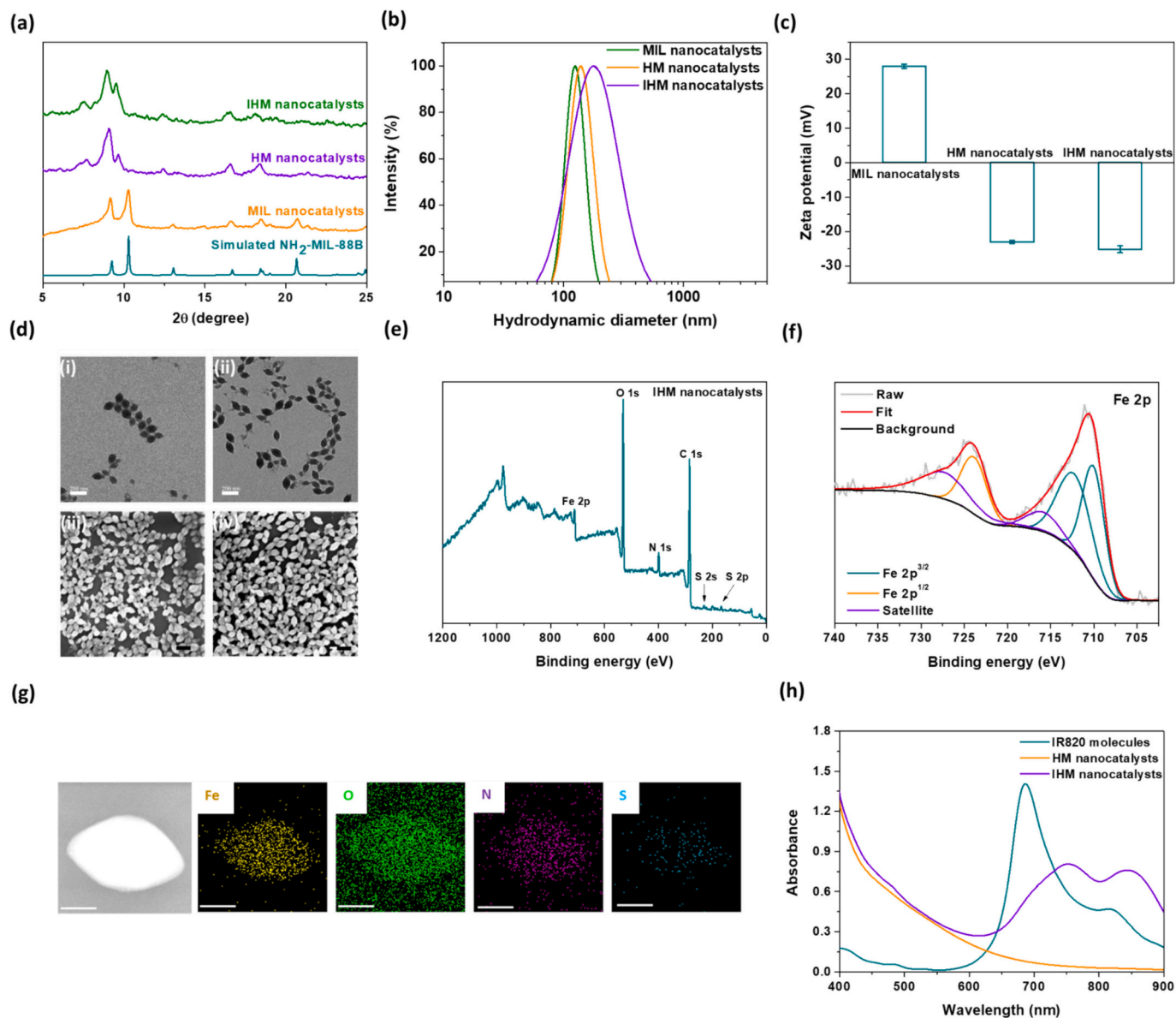


**Fig. 1.** (a) XRD patterns, (b) DLS particle size distribution profiles, and (c) zeta potential values of MIL, HM, and IHM nanocatalysts. (d) TEM (top) and SEM (bottom) images of HM ((i) and (iii)) and IHM nanocatalysts ((ii) and (iv)). Scale bars are 200 nm. (e) XPS spectrum and (f) Fe 2p XPS spectra of IHM nanocatalysts. (g) Elemental mapping images of IHM nanocatalysts. Scale bars are 50 nm. (h) UV/Vis spectra of free IR820 molecules, HM nanocatalysts, and IHM nanocatalysts in 0.9 % saline solution.

## 2.26. Statistical analysis

All data were expressed as mean  $\pm$  standard deviation (SD) for 3 independent experiments. The differences ( $p$ -value) among groups were determined using one-way ANOVA analysis or one-tailed Student's  $t$ -test. Statistical significance was defined as  $*p < 0.05$ ,  $**p < 0.01$ ,  $***p < 0.001$ , and  $p > 0.05$  was no significant difference (ns).

**Table 1**

DLS data and IR820 loading characteristics of various nanocatalysts.

Sample	$D_h$ (nm)	PDI	DLE (%)	DLC (wt%)
MIL nanocatalysts	124.4 $\pm$ 2.0	0.071 $\pm$ 0.030	–	–
HM nanocatalysts	136.5 $\pm$ 4.4	0.105 $\pm$ 0.008	–	–
IHM nanocatalysts	173.3 $\pm$ 9.6	0.220 $\pm$ 0.044	94.4 $\pm$ 1.2	19.2 $\pm$ 0.2

## 3. Results and discussion

### 3.1. Synthesis and characterization of IHM nanocatalysts

The detailed synthetic route of IHM nanocatalysts was presented in [Scheme 1a](#). First, MIL nanocatalysts from the coordination of  $\text{FeCl}_3$  molecules with BDC- $\text{NH}_2$  ligands were fabricated under DMF-free conditions using a mild method instead of the traditional hydrothermal process [42]. The XRD pattern of MIL nanocatalysts is similar to that of the simulated one, indicating the successful synthesis ([Fig. 1a](#)). Moreover, the MIL nanocatalysts dispersed in deionized water were characterized by DLS to exhibit a mean hydrodynamic diameter ( $D_h$ ) of ca 124.4 nm and narrow size distribution (PDI ca 0.07) ([Table 1](#) and [Fig. 1b](#)). As shown in SEM and TEM images ([Fig. S3](#)), the MIL nanocatalysts had a well-dispersed spindle-like shape, with a diameter ranging from 150 to 200 nm. Notably, after being dispersed in 0.9 % saline aqueous solution at 37 °C mimicking physiological salt condition,

the MIL nanocatalysts showed considerably enlarged particle size (over 4000 nm) and visible precipitation (Fig. S4), indicating the occurrence of serious inter-particle aggregation. Such an inter-particle aggregation of MIL nanocatalysts is not beneficial for their application in tumor-targeted drug delivery. To improve the colloidal stability of MIL nanocatalysts in a physiological environment and endow MIL nanocatalysts with specific tumor targeting, HA, a natural polysaccharide capable of targeting CD44-overexpressed cancer cells, was covalently decorated on the surfaces of MIL nanocatalysts through NHS/EDC-mediated amidation between carboxyl group-rich HA segments and BDC-NH<sub>2</sub> ligands (Scheme 1a). As shown in Fig. S5, in addition to the characteristic absorption bands of C—N stretching vibration of the benzene ring and the out-of-plane bending vibration of the C—H bond at 1236 cm<sup>-1</sup> and 756 cm<sup>-1</sup>, respectively, and that of Fe-O-Fe tensile vibration at 531 cm<sup>-1</sup> from MIL nanocatalysts, the absorption bands of C—O stretching vibration in the saccharide structure of HA at ~1045 cm<sup>-1</sup> was observed in the FT-IR spectrum of HM nanocatalysts, confirming the successful conjugation of HA segments on the surfaces of MIL nanocatalysts. Also, compared to MIL nanocatalysts with positive zeta potential (ca +28 mV), the HM nanocatalysts exhibited considerably negative zeta potential values (ca -23.1 mV) owing to the surface decoration of carboxylic acid-rich HA segments (Fig. 1c). Moreover, the particle size (ca 136.5 nm) of HM nanocatalysts was somewhat larger than that (124.4 nm) of MIL nanocatalysts due to the presence of an HA-constituted coating layer (Table 1 and Fig. 1b). A thin HA layer of ca 6.6 nm was also observed at the surface of HM nanocatalysts (Fig. S6). Notably, the MIL nanocatalysts after HA modification still preserved the integral crystalline structure and spindle-like shape as presented in the XRD, SEM, and TEM characterization (Fig. 1a and d), illustrating that the HA coating did not impact the construction of MIL nanocatalysts. After being transferred from deionized water to 0.9 % saline solution, distinct from the largely increased particle size and visible precipitates of the MIL nanocatalysts, the virtually unchanged particle size and sound

suspension for HM nanocatalysts were attained (Fig. S4). This suggests that the hydrophilic and negatively charged HA coating of HM nanocatalysts could effectively prevent interparticle flocculation to enhance their colloidal stability. Therefore, the HM nanocatalysts were utilized as IR820 vehicles for tumor treatment of combined phototherapy (PTT and PDT) and chemodynamic therapy.

The IHM nanocatalysts were attained through multiple  $\pi$ - $\pi$  stacking, hydrophobic, and coordination interactions of IR820 molecules with BDC ligands and Fe<sup>3+</sup> ions of HM nanocatalysts. The encapsulation of IR820 molecules into HM nanocatalysts somewhat enlarged the particle size from ca 136.5 to 173.3 nm (Table 1 and Fig. 1b). As presented in Fig. 1e, the XPS spectrum of IHM nanocatalysts showed the characteristic peaks of S 2s and S 2p at ca 240 and 175 eV, respectively, proving the effective incorporation of IR820 molecules into HM nanocatalysts. Note that the XRD pattern of IHM nanocatalysts was comparable to that of HM nanocatalysts (Fig. 1a), revealing that the HM nanocatalysts retained their crystalline structure after IR820 encapsulation. Also, as shown in TEM and SEM images (Fig. 1d), the IHM nanocatalysts have a spindle-like shape similar to HM nanocatalysts. Notably, the Fe 2p XPS spectrum of IHM nanocatalysts showed two binding energy peaks at 710.3, 712.7, and 716.3 eV corresponding to the Fe 2p<sup>3/2</sup> main peak and its satellite of Fe<sup>3+</sup>, and the peaks located at 724.1 and 728.1 eV ascribed to the Fe 2p<sup>1/2</sup> main peak and its satellite of Fe<sup>3+</sup> (Fig. 1f), confirming that IR820 incorporation did not affect the existence of ferric ions. The EDS images further illustrate that IR820 molecules and ferric ions were evenly distributed in the IHM nanocatalysts (Fig. 1g), and the IR820 loading content was quantified by UV/Vis measurement to be around 19.2 wt% (Table 1). The Fe<sup>3+</sup> content of IHM nanocatalysts determined by ICP-AES is ca 35.2 wt%. Furthermore, the IHM nanocatalysts dispersed in 10 % FBS-containing saline solution or DMEM medium at 37 °C exhibited nearly unchanged particle size for 24 h (Fig. S7a). After being stored in deionized water at 4 °C for 21 days, the IHM nanocatalysts retained virtually unvaried particle size and size distribution

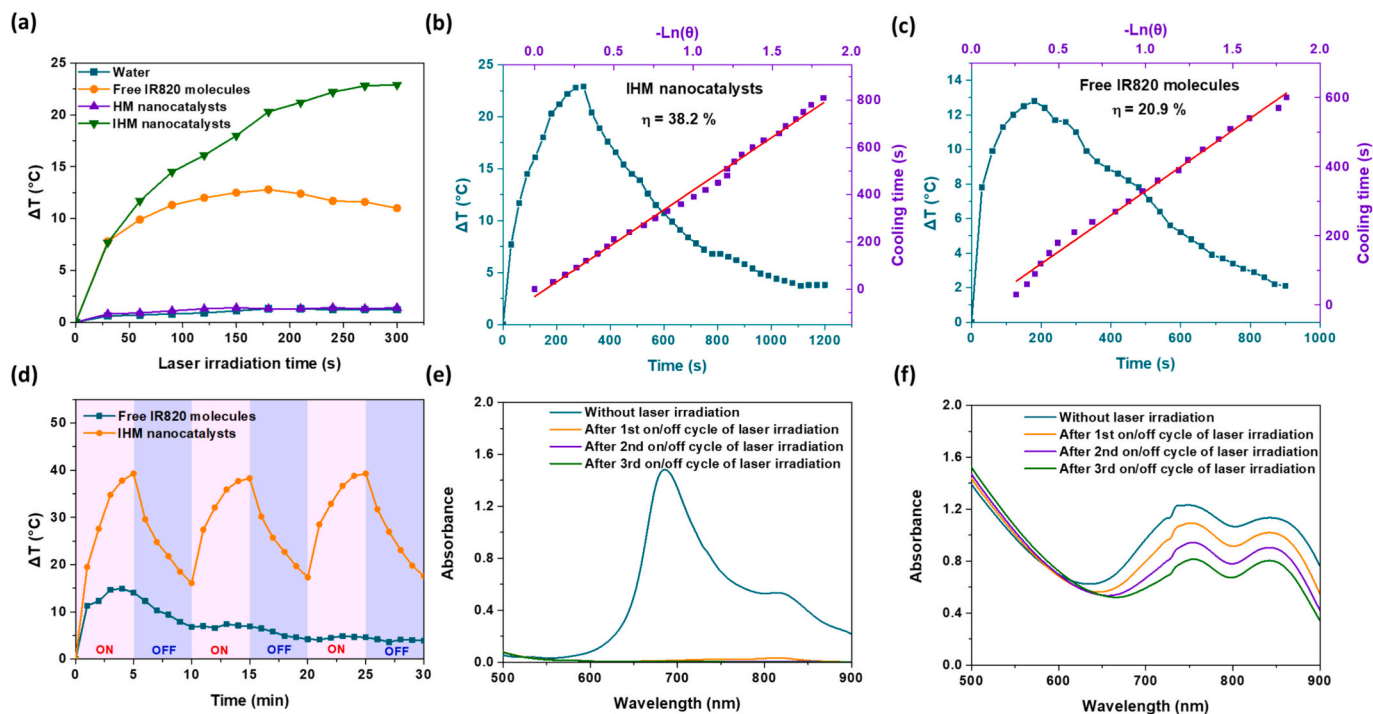


**Fig. 2.** (a) Temperature elevation profiles of free IR820 molecules, HM nanocatalysts, and IHM nanocatalysts in 0.9 % saline aqueous solution (IR820 concentration: 11.8  $\mu\text{g}/\text{mL}$ ) exposed to irradiation of 808 nm NIR laser (1.0  $\text{mW}/\text{cm}^2$ ). Temperature change profile of (b) IHM nanocatalyst and (c) free IR820 molecule solution (IR820 concentration: 11.8  $\mu\text{g}/\text{mL}$ ) after exposure to 808 nm laser irradiation (1.0  $\text{W}/\text{cm}^2$ ) for single on/off cycle, and plot of cooling time versus negative logarithm of the temperature driving force. (d) Temperature change of aqueous solutions containing free IR820 molecules or IHM nanocatalysts (IR820 concentration: 16.5  $\mu\text{g}/\text{mL}$ ) exposed to three on/off cycles of 808 nm NIR laser irradiation (1.0  $\text{W}/\text{cm}^2$ ). UV/Vis spectra of (e) free IR820 molecules and (f) IHM nanocatalysts in 0.9 % saline aqueous solution after NIR laser irradiation of repeated on/off cycles.

(Fig. S7b). These results suggest the excellent colloidal stability of IHM nanocatalysts. Interestingly, when the IR820 molecules were encapsulated into HM nanocatalysts, the characteristic absorption of IR820 molecules showed a remarkable red shift (Fig. 1h), being ascribed to the extensive hydrophobic and  $\pi$ - $\pi$  stacking interaction as well as  $\text{Fe}^{3+}$ -mediated chelation between IR820 molecules and HM nanocatalysts. Such a red shift in the absorption of IR820 molecules encapsulated within nanoparticles was also reported elsewhere [39,43].

### 3.2. Photothermal activity and stability of IHM nanocatalysts

The photothermal capability and stability of IHM nanocatalysts in saline solution exposed to 808 nm NIR laser irradiation were evaluated by measuring the temperature variation of the solution with an infrared thermal imaging camera. As presented in Fig. 2a, during NIR laser irradiation (1.0 W/cm<sup>2</sup> for 300 s), different from saline solution and HM nanocatalyst solution without significant temperature elevation, the aqueous solutions containing IR820 molecules or IHM nanocatalysts (IR820 concentration = 11.8  $\mu\text{g}/\text{mL}$ ) showed the appreciably raised temperature. Notably, at the same IR820 concentration, the temperature elevation of the IHM nanocatalyst solution was markedly higher than that of the IR820 solution. Based on the photothermal heating-cooling curves (Fig. 2b and c), the photothermal conversion efficiency ( $\eta$ ) of IHM nanocatalysts was attained to be ca 38.2 %, being profoundly higher compared to that of free IR820 molecules (ca 20.9 %). This could be ascribed to that the IR820 absorption of IHM nanocatalysts was significantly shifted to approach the central wavelength (808 nm) of the NIR laser used in this work (Fig. 1h), thus enhancing their absorbing NIR ability and photothermal effect. Moreover, the temperature elevation of IHM nanocatalyst solution under NIR laser irradiation was appreciably promoted by increasing nanoparticle concentration (from 25 to 100  $\mu\text{g}/\text{mL}$ ) or the power density of NIR laser irradiation (from 0.5 to 1.5 W/cm<sup>2</sup>) (Fig. S8). It should be mentioned that the IHM nanocatalysts exhibited a higher photothermal conversion efficiency compared to other previously reported IR820-carrying nanoparticles, such as IR820-paclitaxel assemblies (28.4 %) [40], IR820 functionalized melanin

nanoplates (24.7 %) [44] and IR820-loaded oxyhemoglobin (16.6 %) [39]. This signifies that the encapsulation of IR820 molecules into HM nanocatalysts by multiple interactions could enhance their photothermal conversion efficacy. More importantly, after three on/off cycles of NIR laser irradiation, free IR820 molecules showed a largely declined photothermal effect, while the IHM nanocatalysts still maintained satisfied photothermal capability (Fig. 2d). Even receiving five on/off cycles of NIR laser irradiation, the IHM nanocatalysts showed prominent photothermal performance (Fig. S9). Moreover, after three on/off cycles of NIR laser irradiation, the absorbance of free IR820 molecules in the wavelength range of 600–850 nm was considerably reduced compared to that of IHM nanocatalysts (Fig. 2e and f). These results suggest that the developed IHM nanocatalysts exhibit robust photothermal effects and decline the photobleaching of IR820, thus being favorable to enhancing the anticancer potency of IR820-based phototherapy.

### 3.3. GSH-elicited disintegration and payload release of IHM nanocatalysts

Considering that the cancer cells exhibit a weakly acidic (pH 4.5–6.0) and GSH-rich (2–10 mM) intracellular milieu, and GSH can reduce  $\text{Fe}^{3+}$  ions to  $\text{Fe}^{2+}$  ions, the structure conversion of IHM nanocatalysts in response to pH change and GSH existence was investigated. As revealed in Fig. 3a, for Phe solution containing IHM nanocatalysts (50  $\mu\text{g}/\text{mL}$ ) and GSH (0.4 mM), the absorbance at 509 nm was largely enhanced. In contrast, no significant absorption was found in the group of IHM nanocatalysts-treated Phe in the absence of GSH. As the important control, Phe on the treatment with  $\text{Fe}^{3+}$  and GSH showed remarkably increased absorbance at 509 nm. These findings prove that GSH can reduce  $\text{Fe}^{3+}$  ions of IHM nanocatalysts to  $\text{Fe}^{2+}$  ions, which react with Phe to produce a stable orange complex with absorption at 509 nm. Notably, in the lack of GSH, the IHM nanocatalysts dispersed in pH 7.4 and 5.0 aqueous solutions exhibited virtually unchanged particle size over 6 h (Fig. S10). In contrast, IHM nanocatalysts showed markedly enlarged particle size in a 10 mM GSH-containing solution of pH 5.0 over time (Fig. 3b). Also, as presented in TEM images (Fig. 3c), the IHM

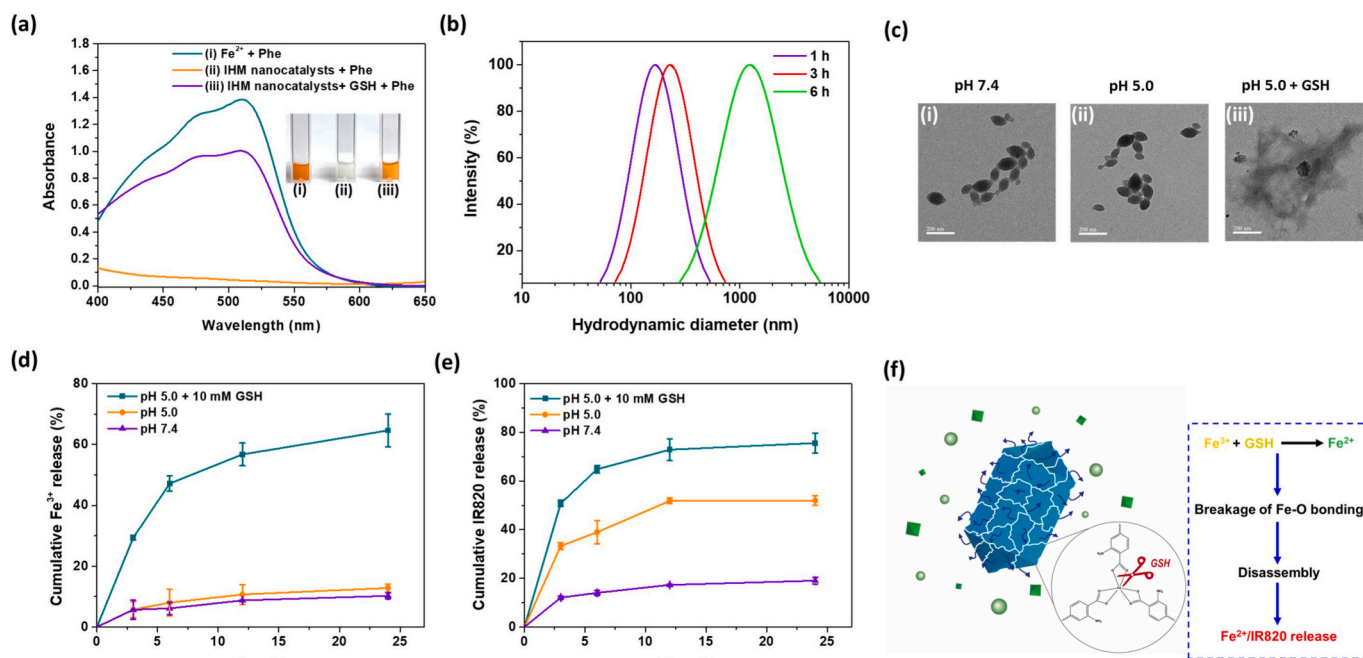


**Fig. 3.** (a) UV/Vis spectra of Phe with different treatments. Inset: photographs of the corresponding samples. (b) DLS particle size distribution profiles of IHM nanocatalysts dispersed in pH 5.0 aqueous solution containing 10.0 mM GSH at different intervals. (c) TEM images of IHM nanocatalysts receiving different treatments. Scale bars are 200 nm. Cumulative release profiles of (d)  $\text{Fe}^{3+}$  and (e) IR820 of IHM nanocatalysts under different conditions. (f) Schematic illustration of GSH-triggered disintegration of IHM nanocatalysts.

nanocatalysts maintained an intact spindle-like shape at pH 7.4 and 5.0 in the lack of GSH. Still, after being treated with a pH 5.0 GSH-containing solution, these nanocatalysts tended to disintegrate into an irregular structure. Furthermore, distinct from remarkable absorption (400–700 nm) of HM nanocatalysts dispersed in pH 5.0 solution for 24 h, no significant absorption of HM nanocatalysts exposed to 10 mM GSH-containing pH 5.0 solutions for 24 h was observed in Fig. S11a. In the presence of GSH, the HM nanocatalysts also showed a visible conversion from a slight orange to a colorless transparent status (Fig. S11b). Based on the above results, it was demonstrated that the GSH-elicited  $\text{Fe}^{3+}$  reduction destroyed the coordination between  $\text{Fe}^{3+}$  ions and BDC- $\text{NH}_2$  ligands, thus leading to the disruption of IHM nanocatalysts. More importantly, while the cumulative release of  $\text{Fe}^{3+}$  from IHM nanocatalysts in pH 7.4 or 5.0 aqueous solutions without GSH was limited to only ca 10 % over a period of 24 h, a significantly promoted  $\text{Fe}^{3+}$  release at pH 5.0 with 10 mM GSH was attained (over 60 %) (Fig. 3d). On the other hand, in the lack of GSH, the cumulative IR820 release of IHM nanocatalysts was promoted in response to the pH change from 7.4 to 5.0 (Fig. 3e). This could be attributed to that the acidity-triggered protonation of indole groups of IR820 declines the  $\pi$ - $\pi$  stacking interaction

of IR820 molecules and IHM nanocatalysts, thus facilitating IR820 outflow. Note that the IR820 liberation from IHM nanocatalysts was further increased in the GSH-containing solution of pH 5.0. Based on the above findings, the GSH-triggered disintegration of IHM nanocatalysts in a weakly acidic milieu could effectively accelerate  $\text{Fe}^{3+}/\text{Fe}^{2+}$  and IR820 release (Fig. 3f), being beneficial to convert intracellular  $\text{H}_2\text{O}_2$  into  $\cdot\text{OH}$  and realize NIR-activated  $^1\text{O}_2$  generation.

### 3.4. GSH depletion and ROS generation

The GSH depletion capability of IHM nanocatalysts was assessed by DTNB as an indicator, which can be reduced by GSH to form yellow TNB with a characteristic absorption at 412 nm [45]. As presented in Fig. 4a, when the reaction time of GSH treated with IHM nanocatalysts was prolonged from 1 to 24 h, the absorbance of the TNB at 412 nm was remarkably decreased. This proves that the IHM nanocatalysts continuously consume GSH via  $\text{Fe}^{3+}$ -induced GSH oxidation (Fig. 4g). Next, TMB that can be oxidized by hydroxyl radicals was used as the probe to evaluate the  $\cdot\text{OH}$ -generating ability of IHM nanocatalysts upon the Fenton reaction. Notably, the increased absorption of oxidized TMB at

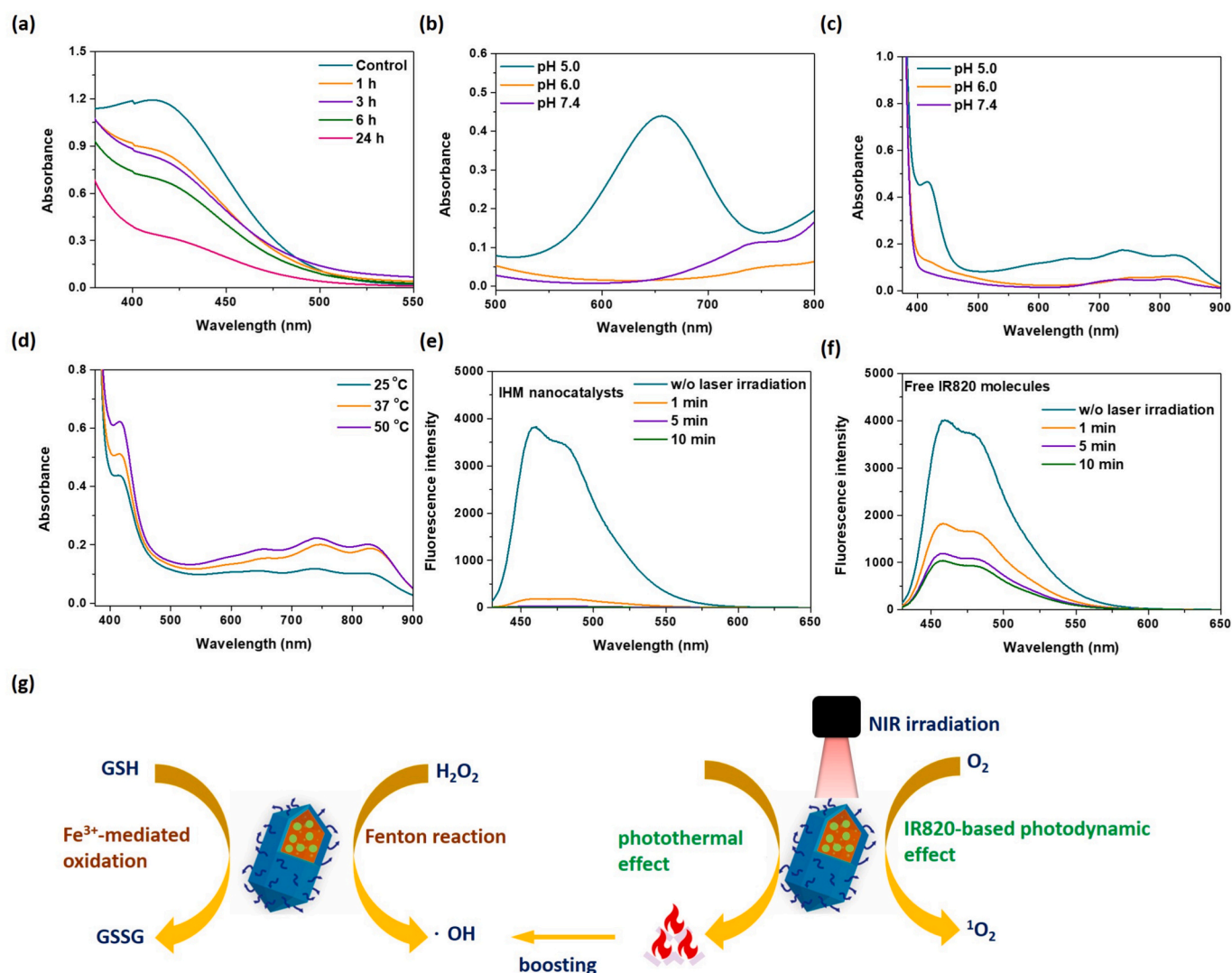


**Fig. 4.** (a) UV/Vis spectra of DTNB molecules dissolved in GSH solution pretreated with IHM nanocatalysts at 37 °C at various time intervals. Absorption spectra of (b) TMB and (c) ABTS treated with IHM nanocatalysts and  $\text{H}_2\text{O}_2$  (100  $\mu\text{M}$ ) at different pH and 37 °C for 10 min (TMB assay) and 1 h (ABTS assay). (d) Absorption spectra of ABTS treated with IHM nanocatalysts and  $\text{H}_2\text{O}_2$  (100  $\mu\text{M}$ ) at different temperatures for 1 h. Fluorescence spectra of DPBF molecules in (e) IHM nanocatalyst and (f) free IR820 solutions receiving 808 nm laser irradiation (1.0  $\text{W}/\text{cm}^2$ ) of various irradiation times. (g) Schematic illustration of GSH depletion, acidity/thermo-augmented  $\cdot\text{OH}$  production, and NIR-triggered  $^1\text{O}_2$  production of IHM nanocatalysts.

652 nm was observed in pH 5.0 aqueous solutions containing IHM nanocatalysts and  $\text{H}_2\text{O}_2$ , while no significant absorption was attained in pH 6.0 or 7.4 aqueous solutions containing the counterparts (Fig. 4b). Also, the  $\cdot\text{OH}$ -generating ability was assessed by employing ABTS. With the solution pH being adjusted from pH 7.4 to 5.0, the absorption of oxidized ABTS from visible light to NIR light was appreciably enhanced in the IHM nanocatalysts plus  $\text{H}_2\text{O}_2$  group (Fig. 4c). These results suggest that the IHM nanocatalysts under weakly acidic conditions could promote the conversion of  $\text{H}_2\text{O}_2$  into  $\cdot\text{OH}$  by the accelerated Fenton reaction rate. A similar acidity-activated Fenton reaction of MOF-based nanoparticles was observed elsewhere [36,46,47]. Furthermore, the absorption of oxidized ABTS in an aqueous solution containing IHM nanocatalysts and  $\text{H}_2\text{O}_2$  was remarkably enhanced with temperature elevation from 25 to 50 °C (Fig. 4d), signifying that the Fenton reaction based on IHM nanocatalysts could be accelerated by increasing reaction temperature, thereby promoting decomposition of  $\text{H}_2\text{O}_2$  into  $\cdot\text{OH}$ . On the other hand, the photo-triggered  $^1\text{O}_2$ -generating performance of IHM nanocatalysts was explored by DPBF, a  $^1\text{O}_2$  indicator that displayed the declined fluorescence intensity at 450–500 nm in the existence of  $^1\text{O}_2$ . With irradiation of 808 nm NIR laser, the fluorescence intensity of DPBF molecules in aqueous solutions containing IHM nanocatalysts or free IR820 molecules (IR820 concentration = 11.8  $\mu\text{g}/\text{mL}$ ) was appreciably decreased with the prolonged irradiation time (Fig. 4e and f), confirming  $^1\text{O}_2$  production from IR820-mediated photodynamic effect. Importantly,

at the same laser irradiation time, the fluorescence intensity of DPBF in the IHM nanocatalyst solution was appreciably lower than that of DPBF in the free IR820 solution. Based on these findings, it was concluded that the IHM nanocatalysts not only enhanced the NIR-triggered  $^1\text{O}_2$ -generating ability of IR820 molecules by relieving photothermal-elicited degradation of IR820 but also exhibited acidity/thermo-augmented  $\cdot\text{OH}$  production via  $\text{Fe}^{3+}/\text{Fe}^{2+}$ -mediated Fenton reaction (Fig. 4g).

### 3.5. In vitro cellular uptake, intracellular $\text{Fe}^{2+}$ generation and GSH depletion

Considering the active targeting of HA segments to CD44-overexpressed cancer cells, the cellular uptake of IHM nanocatalysts by 4 T1 cells with CD44 overexpression was examined by CLSM and flow cytometry. As presented in the CLSM images (Fig. 5a) and quantified IR820 fluorescence intensity (Fig. S12), when the incubation time was prolonged from 1 to 4 h, the intracellular IR820 fluorescence signals of 4 T1 cells treated with IHM nanocatalysts were appreciably enhanced as compared to those of 4 T1 cells incubated with both of IHM nanocatalysts and free HA molecules. The same findings were attained with other CD44-overexpressed TRAMP-C1 cancer cells (Fig. S13a). Also, after 4 h incubation, the data of flow cytometry revealed that the IR820 fluorescence intensity of 4 T1 cells exposed to IHMs nanocatalysts was higher compared to that of cells treated with IHM nanocatalysts and free

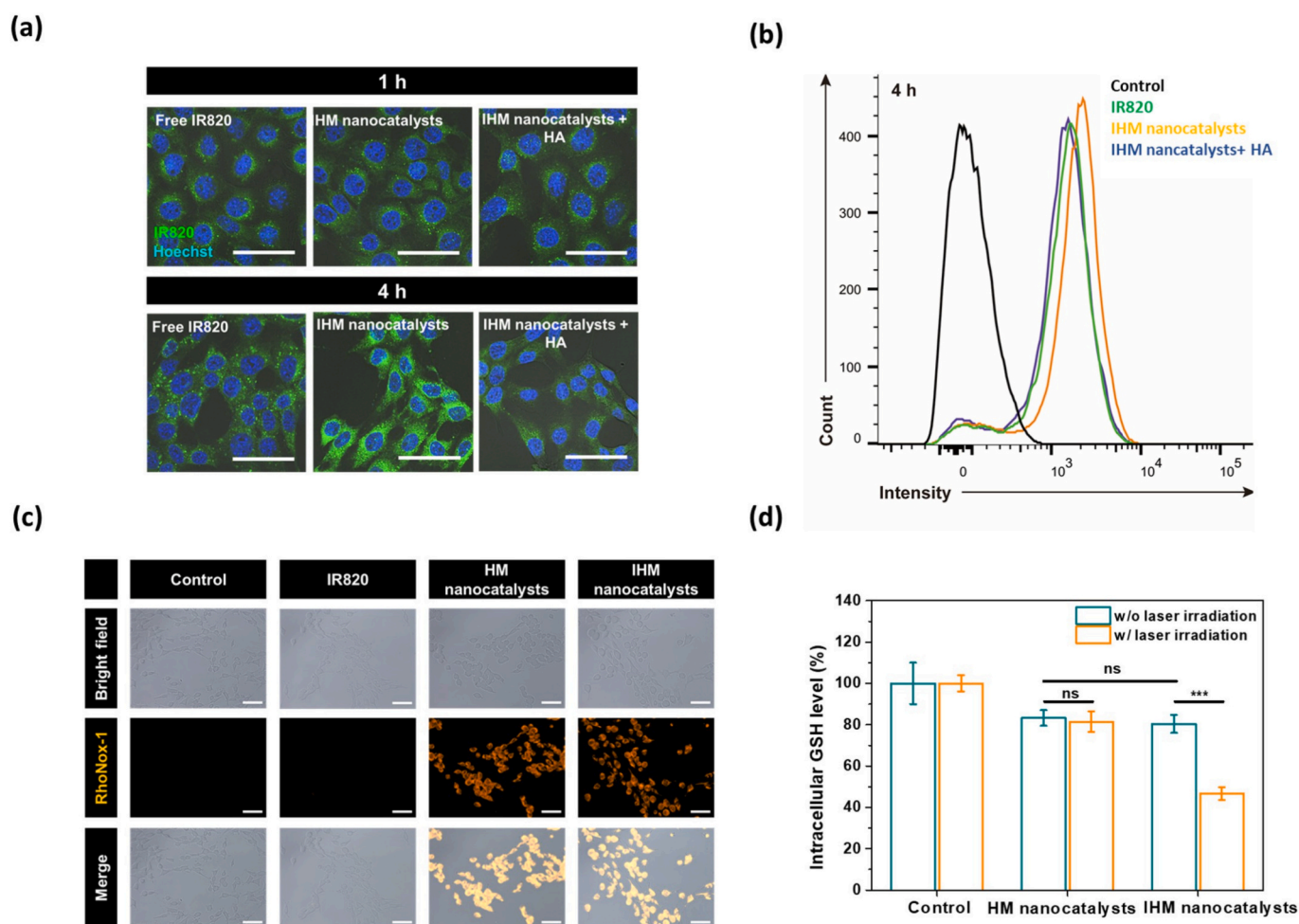


Fig. 5. (a) CLSM images of 4 T1 cells incubated with free IR820 molecules, IHM nanocatalysts, and IHM nanocatalysts plus free HA segments, respectively, for 1 and 4 h. Scale bars are 50  $\mu\text{m}$ . (b) Flow cytometric histograms of 4 T1 cells incubated with free IR820 molecules, IHM nanocatalysts, and IHM nanocatalysts plus free HA segments, respectively, for 4 h. (c) RhoNox-1 staining of 4 T1 cells incubated with free IR820 molecules, HM nanocatalysts, and IHM nanocatalysts, respectively, for 24 h. Scale bars are 50  $\mu\text{m}$ . (d) Intracellular GSH level of 4 T1 cells treated with free IR820 molecules, HM nanocatalysts, or IHM nanocatalysts for 24 h with or without NIR laser irradiation (1.0  $\text{W}/\text{cm}^2$ , 5 min). \* $p < 0.05$ , \*\* $p < 0.01$ , \*\*\* $p < 0.001$ , ns > 0.05.

HA segments (Fig. 5b). These results strongly demonstrate that the IHM nanocatalysts could be efficiently internalized by CD44-overexpressed 4 T1 cells upon CD44-mediated endocytosis. In contrast, the cellular uptake of these nanocatalysts by 4 T1 or TRAMP-C1 cells was hindered in the presence of free HA molecules due to the competition of free HA molecules with nanocatalysts for CD44 receptors of 4 T1 cells. Furthermore, compared to IHM nanocatalysts, free IR820 molecules showed poor cellular uptake by 4 T1 cells. This could be ascribed to that the sulfonate-containing amphiphilic IR820 molecules tended to aggregate into negatively charged particles in a culture medium, thus declining their affinity for negative charge-rich cell membranes to

hinder cellular internalization. Also, similar results regarding the lower cellular uptake of free IR820 molecules than that of IR820-loaded nanoparticles were reported elsewhere [39,40]. Notably, as revealed in the RhoNox-1 staining images (Fig. 5c), distinct from PBS- (control) or free IR820 molecules-treated 4 T1 cells without significant fluorescence signals, 4 T1 cells incubated with IHM or HM nanocatalysts displayed a bright orange fluorescence. This suggests that the intracellular GSH leads to the disintegration of these nanoparticles to release  $\text{Fe}^{3+}$  ions, followed by GSH-mediated reduction of  $\text{Fe}^{3+}$  into  $\text{Fe}^{2+}$  ions. These results agree with these findings regarding the GSH-triggered  $\text{Fe}^{3+}$  release from the disassembly of IHM nanocatalysts at pH 5.0 (Fig. 3c and d) and

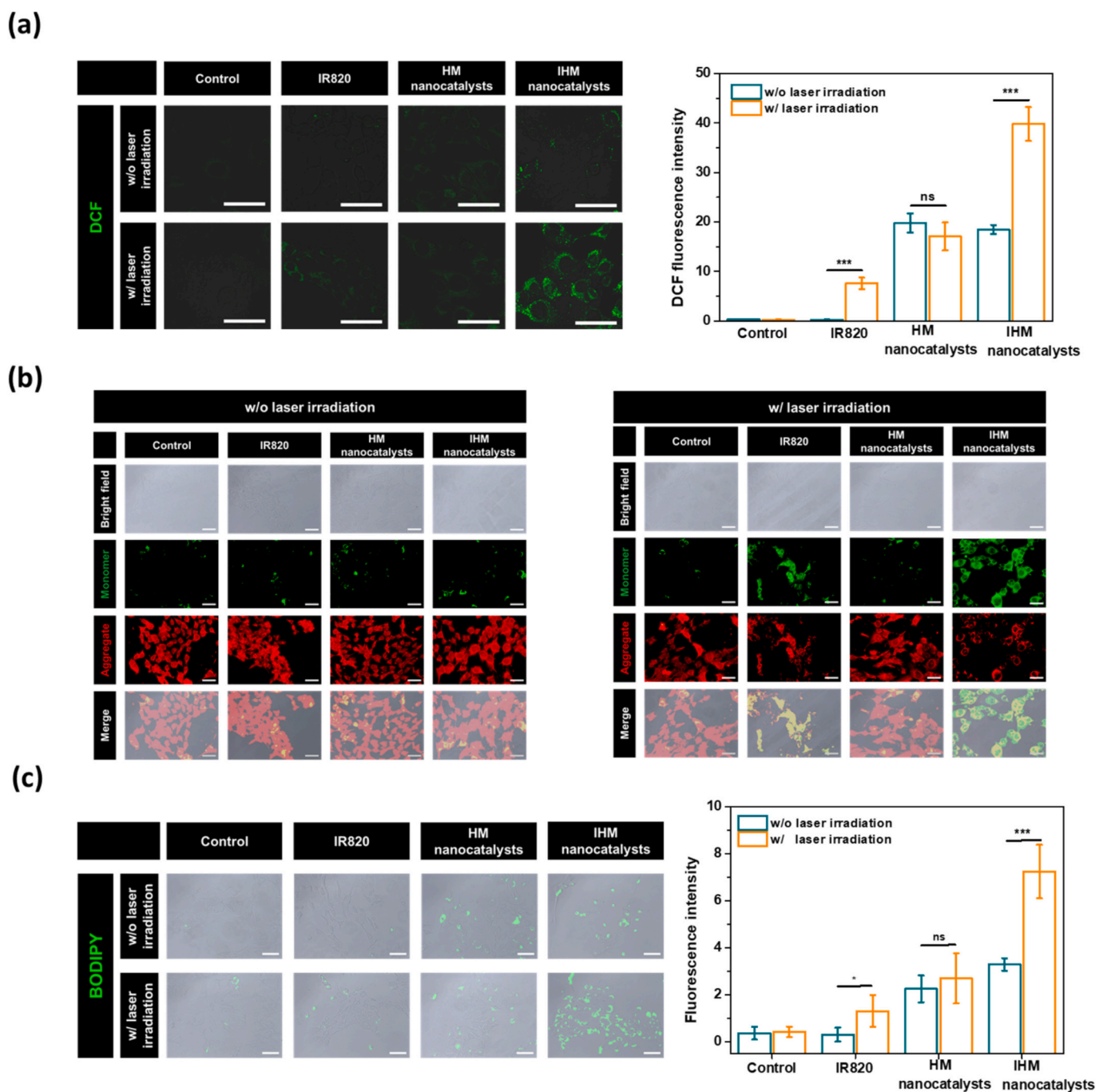


Fig. 6. (a) DCF fluorescence images and quantification analysis of 4 T1 cells receiving different formulations with or without laser irradiation ( $1.0 \text{ W/cm}^2$ , 5 min). Scale bars are  $50 \mu\text{m}$ . (b) JC-1 staining of 4 T1 cells receiving various treatments (JC-1 aggregates emit red fluorescence, and JC-1 monomers emit green fluorescence). Scale bars are  $50 \mu\text{m}$ . (c) BODIPY<sup>581/591</sup> staining and quantification analysis of 4 T1 cells receiving various treatments. Scale bars are  $50 \mu\text{m}$ . \* $p < 0.05$ , \*\* $p < 0.01$ , \*\*\* $p < 0.001$ , ns  $> 0.05$ . (For interpretation of the references to colour in this figure legend, the reader is referred to the web version of this article.)

the GSH-induced  $\text{Fe}^{3+}$  reduction evidenced by Phe assay (Fig. 3a). On the other hand, in the absence of NIR laser irradiation, for HM nanocatalysts with or without IR820 payloads, the  $\text{Fe}^{3+}$ -elicited GSH oxidation somewhat declined the intracellular GSH level of the treated 4 T1 cells by 20 % (Fig. 5d). With NIR laser irradiation, the intracellular GSH level of 4 T1 cells incubated with IHM nanocatalysts was largely decreased to below 50 % compared to that of cells receiving HM nanocatalysts. Undoubtedly, the endocytosed IHM nanocatalysts exposed to NIR laser irradiation could generate  $^1\text{O}_2$  based on the IR820-mediated photodynamic effect and promote  $\cdot\text{OH}$  production upon the thermo-enhanced Fenton reaction, thereby consuming endogenous GSH in an oxidation manner.

### 3.6. Intracellular ROS generation, mitochondrial damage, and LPO production

DCFH-DA was used as the ROS probe to evaluate the intracellular ROS generation of 4 T1 cells incubated with IHM nanocatalysts. In the lack of NIR irradiation, no significant DCF fluorescence in 4 T1 cells exposed to free IR820 molecules was observed (Fig. 6a), whereas weak DCF fluorescence signals of 4 T1 cells receiving HM nanocatalysts with or without IR820 payloads were attained owing to the formation of a few intracellular  $\cdot\text{OH}$  upon the Fenton reaction between HM nanocatalysts and endogenous  $\text{H}_2\text{O}_2$ . With 808 nm NIR laser irradiation, 4 T1 cells treated with IHM nanocatalysts exhibited considerable DCF fluorescence compared to cells treated with HM nanocatalysts or free IR820 molecules (Fig. 6a). According to the semi-quantitative data of DCF fluorescence images, after laser irradiation, the IHM nanocatalyst group showed a 2.4-fold and 5.1-fold increase in the intracellular DCF intensity signals compared to the HM nanocatalyst group and free IR820 group. Obviously, the internalized IHM nanocatalysts with laser irradiation boosted the  $\cdot\text{OH}$  generation by hyperthermia-augmented Fenton reaction and produced  $^1\text{O}_2$  via IR820-mediated photodynamic effect, thus profoundly raising intracellular ROS level. By contrast, in the lack of IR820, the HM nanocatalysts with or without NIR laser irradiation only generated limited  $\cdot\text{OH}$  via the Fenton reaction, unable to sufficiently increase intracellular ROS. Moreover, the poor cellular uptake and serious photobleaching of free IR820 molecules largely declined intracellular  $^1\text{O}_2$  production under laser irradiation.

Several studies demonstrate that mitochondria damage is a key and characteristic mark of ROS-associated apoptosis [33,48]. To determine the change of mitochondrial transmembrane potential induced by IHM nanocatalysts, the cell damage was tested with a JC-1 staining assay. As presented in Fig. 6b, in the absence of NIR laser irradiation, 4 T1 cells incubated with HM or IHM nanocatalysts exhibited remarkable red fluorescence similar to the control and free IR820 groups. This indicates that minor  $\cdot\text{OH}$  produced from HM or IHM nanocatalysts could not effectively damage mitochondria, thus enabling JC-1 to diffuse into the mitochondrial matrix through the mitochondrial membrane and form aggregates emitting red fluorescence. Notably, with NIR laser irradiation, massively visible green fluorescence was observed in the IHM nanocatalyst-treated 4 T1 cells, while only some green fluorescence was found in 4 T1 cells incubated with free IR820 molecules. Also, the ratio of JC-1 green and red fluorescence intensity from 4 T1 cells treated with IHM nanocatalysts is remarkably 2.75-fold higher than that of cells incubated with free IR820 molecules (Fig. S14). These findings demonstrate that the strong ROS storm composed of  $^1\text{O}_2$  and  $\cdot\text{OH}$  generated from the internalized IHM nanocatalysts exposed to NIR laser irradiation could potentially destroy mitochondria, thereby promoting the transformation of JC-1 into a monomer emitting green fluorescence. By contrast, 4 T1 cells treated with free IR820 molecules and laser irradiation showed only partial mitochondria damage due to slight intracellular  $^1\text{O}_2$  production. Furthermore, the observed weak green fluorescence for the HM nanocatalyst-treated 4 T1 cells with NIR laser irradiation signifies that the internalized HM nanocatalysts could not generate sufficient  $\cdot\text{OH}$  to damage mitochondria without the assistance

of the IR820-based hyperthermia.

In addition to mitochondria damage, intracellular LPO formation elicited by excess ROS has been demonstrated to lead to ferroptosis, a type of iron-dependent nonapoptotic cell death [19,49,50]. The BOD-IPY<sup>581/591</sup> as a probe was used to examine the LPO generation within 4 T1 cells treated with IHM nanocatalysts and laser irradiation. With NIR laser irradiation, 4 T1 cells incubated with IHM nanocatalysts displayed stronger green fluorescence signals than cells treated with free IR820 molecules or HM nanocatalysts (Fig. 6c). In contrast, 4 T1 cells receiving HM or IHM nanocatalysts without NIR laser irradiation had weak green fluorescence signals. These results signify that the IHM nanocatalysts could effectively enhance the intracellular accumulation of toxic LPO by NIR-triggered  $^1\text{O}_2$  production in combination with thermal-enhanced  $\text{Fe}^{3+}/\text{Fe}^{2+}$ -mediated  $\cdot\text{OH}$  generation, while free IR820 molecules exposed to laser irradiation only cause limited LPO formation owing to the intracellular insufficient  $^1\text{O}_2$  accumulation. In view of the above findings, we expected that the IHM nanocatalysts efficiently internalized by CD44-overexpressed cancer cells could not only largely destroy mitochondrial and product LPO by NIR-activated powerful redox homeostasis disturbance but also ablate cancer cells via NIR-triggered hyperthermia, thereby boosting ferroptosis combined with photo/CDT-mediated anticancer efficacy.

### 3.7. In vitro anticancer efficacy of combined phototherapy and CDT

To investigate the anticancer effect of IR820-based phototherapy combined with HM nanocatalysts-triggered CDT, the viability of 4 T1 cells treated with IHM nanocatalysts was determined by MTT assay. As revealed in Fig. 7a, in the absence of NIR laser irradiation, 4 T1 cells incubated with free IR820 molecules, HM, or IHM nanocatalysts maintained high cell viability (over 90 %). A similar result was also attained in WS1 cells (Fig. S15). These findings reveal that, without laser irradiation, single CDT delivered by HM and IHM nanocatalysts showed low cytotoxicity on the cancer and normal cells. With NIR laser irradiation, the viability of 4 T1 cells treated with free IR820 molecules or IHM nanocatalysts was remarkably reduced in the IR820 concentration-dependent manner (Fig. 7b). In contrast, no significant decrease in the viability of 4 T1 cells receiving HM nanocatalysts was attained. Notably, at the low IR820 concentrations (e.g. 1.48 and 2.95  $\mu\text{g}/\text{mL}$ ), the IHM nanocatalysts with laser irradiation exhibited anticancer capability superior to free IR820 molecules. Similarly, with NIR laser irradiation, compared to free IR820 molecules, the IHM nanocatalysts potently inhibited the proliferation of TRAMP-C1 cells (Fig. S13b). The fluorescence staining of live/dead 4 T1 cells showed that most of the 4 T1 cells exposed to IHM nanocatalysts combined with 5-min NIR laser irradiation displayed quite intense PI signals in comparison with cells treated with the counterparts without NIR laser irradiation or free IR820 molecules with NIR laser irradiation (Fig. 7c). These results strongly demonstrate that the IHM nanocatalysts internalized by 4 T1 cells upon CD44-mediated endocytosis could effectively cause apoptosis and ferroptosis by NIR-triggered hyperthermia and  $^1\text{O}_2$  production in combination with  $\text{Fe}^{3+}/\text{Fe}^{2+}$ -mediated  $\cdot\text{OH}$  generation. In contrast, the poor cellular uptake, insufficient  $^1\text{O}_2$  production, remarkable photobleaching, and weak hyperthermia of free IR820 molecules limited their phototherapy-based anticancer efficacy.

### 3.8. Induction of ICD by IHM nanocatalysts upon NIR laser irradiation

Recently, PTT, PDT, and CDT have been demonstrated to cause ICD [6,7,51–53]. ICD supplies a novel activation method of the T cells in immunotherapy. DAMPs, such as secreted ATP, exposed CRT and released HMGB1, can mediate the immunogenic characteristics of ICD [6,7,51–53]. As shown in Fig. 7d and S16, compared to free IR820 and HM nanocatalyst groups, the IHM nanocatalyst group with laser irradiation exhibited the highest CRT expression, illustrating that the combination of phototherapy and CDT effectively promoted CRT

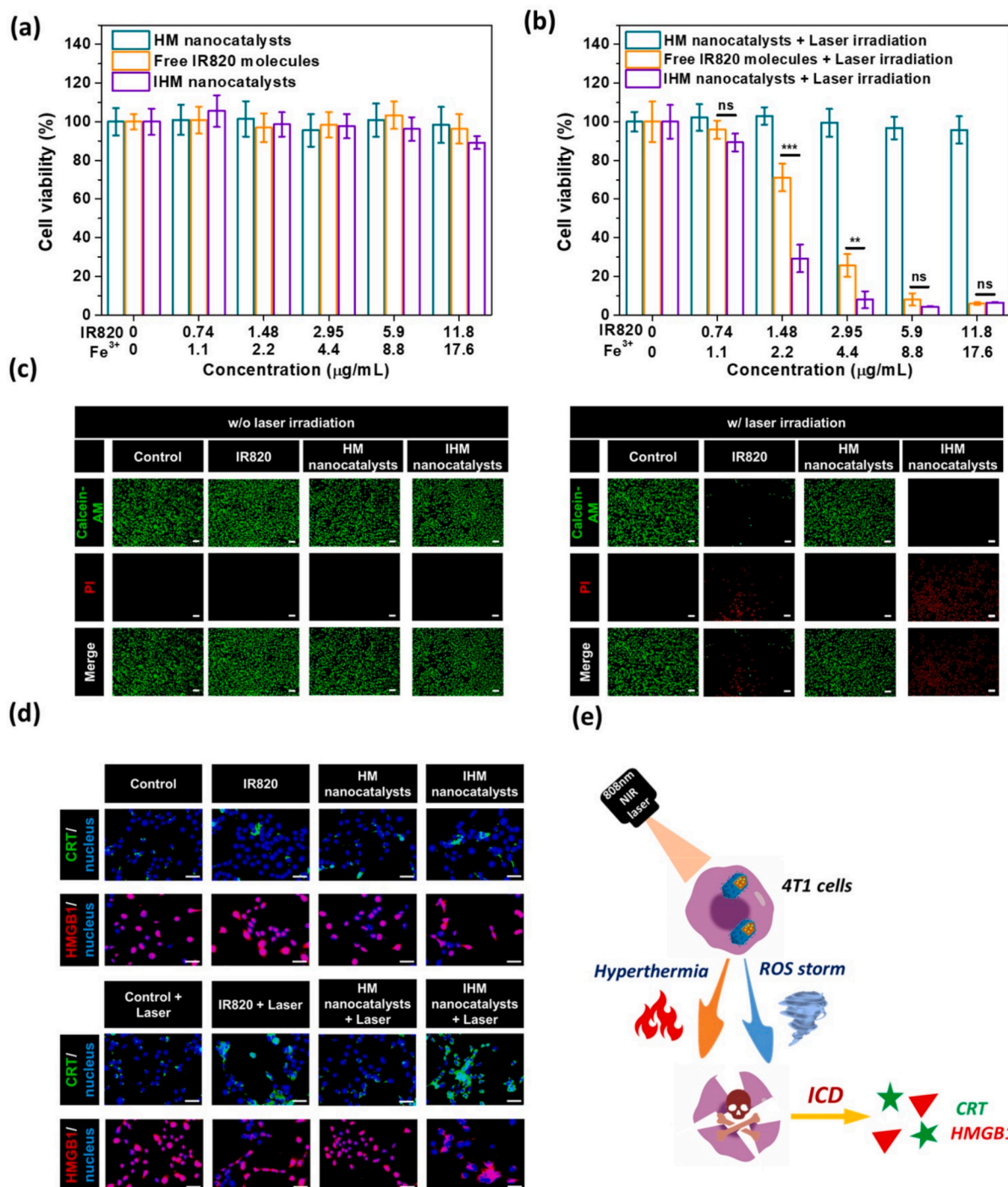


**Fig. 7.** Cell viability of 4 T1 cells treated with free IR820 molecules, HM nanocatalysts, and IHM nanocatalysts without laser irradiation (a) or with laser irradiation (b). (c) Live/death staining analysis of 4 T1 cells receiving different treatments. The viable cells were stained green with calcein-AM, and the dead cells were stained red with PI. Scale bars are 200  $\mu\text{m}$ . (d) CRT and HMGB1 staining of 4 T1 cells receiving various treatments. Scale bars are 50  $\mu\text{m}$ . (e) Schematic illustration of ICD from the hyperthermia and ROS storm generated by IHM nanocatalysts under NIR laser irradiation. \* $p < 0.05$ , \*\* $p < 0.01$ , \*\*\* $p < 0.001$ , ns  $> 0.05$ . (For interpretation of the references to colour in this figure legend, the reader is referred to the web version of this article.)

exposure. To our knowledge, HMGB1 released from the cell nucleus in dying cells can activate inflammation, attract various immune cells, and elicit DC maturation [34,54]. Note that the IHM nanocatalyst-treated 4 T1 cells with laser irradiation showed a significant translocation of HMGB1 from the nuclei to the extracellular space compared to cells receiving various treatments (Fig. 7d). Based on these findings, it is expected that the promoted CRT exposure and HMGB1 liberation by combined phototherapy and CDT of IHM nanocatalysts could activate an

antitumor immune response for inhibition of tumor growth and metastasis.

### 3.9. In vivo tumor accumulation and biodistribution and NIR-triggered tumor hyperthermia

The in vivo tumor accumulation and biodistribution of IHM nanocatalysts were further investigated using the subcutaneous 4 T1 tumor

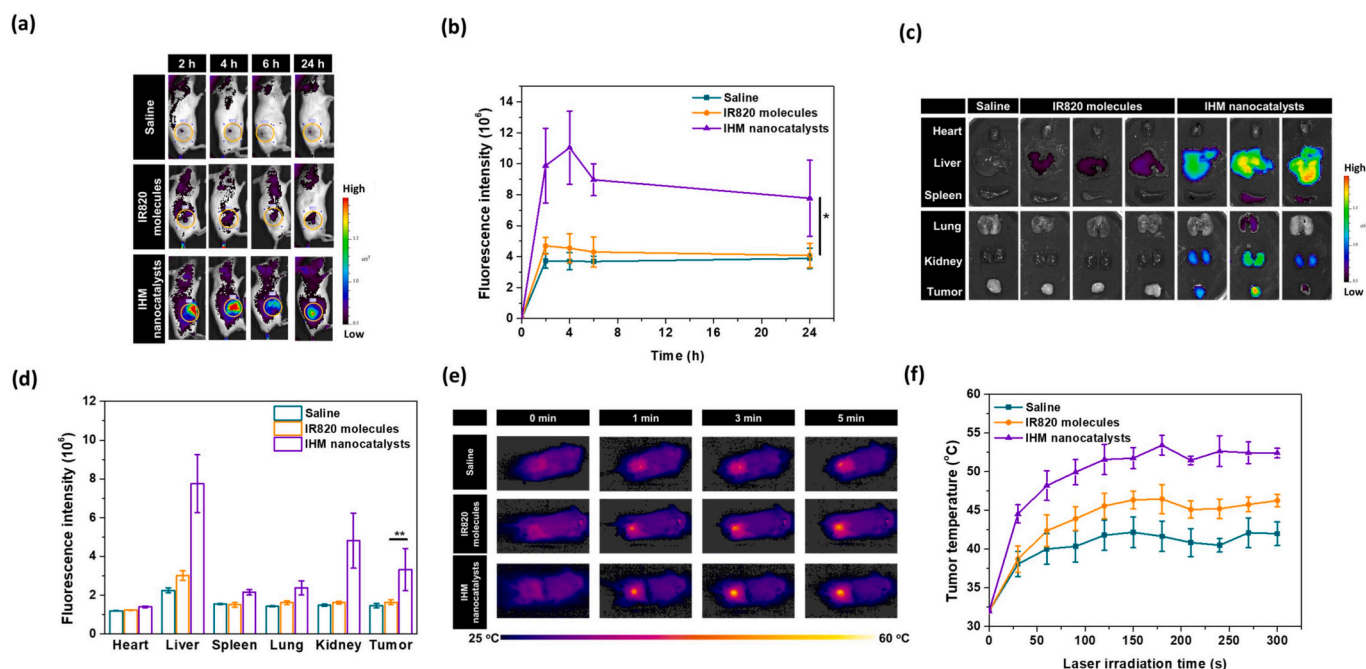


**Fig. 8.** (a) In vivo NIR fluorescence images and (b) IR820 fluorescence signals of 4 T1 tumor-bearing mice intravenously injected with 0.9 % normal saline as the control, free IR820 molecules or IHM nanocatalysts. The tumor sites were marked with yellow circles. (c) NIR fluorescence images and (d) average IR820 fluorescence intensities of tumors and major organs at 24 h post-injection with free IR820 molecules and IHM nanocatalysts, respectively. (e) Infrared thermographic images and (f) temperature elevation profiles of the tumor sites of 4 T1 tumor-bearing mice treated with 0.9 % saline solution, free IR820 molecules or IHM nanocatalysts and irradiated with 808 nm NIR laser ( $1.0 \text{ W/cm}^2$ ) for 5 min at 4 h post-injection. \* $p < 0.05$ , \*\* $p < 0.01$ , \*\*\* $p < 0.001$ , ns  $> 0.05$ . (For interpretation of the references to colour in this figure legend, the reader is referred to the web version of this article.)

model in female BALB/c mice. Upon intravenous injection with free IR820 molecules as the control and IHM nanocatalysts (IR820 dosage:  $1.0 \text{ mg/kg}$ ), the in vivo IR820 fluorescence images of the treated 4 T1 tumor-bearing mice were attained at different time intervals. Note that the IR820 fluorescence intensity in the tumor sites of the IHM nanocatalyst group was appreciably higher than that of the free IR820 group during the identical time period (Fig. 8a and b). Furthermore, at 4 h post-injection, the IHM nanocatalysts exhibited maximized tumor accumulation, as reflected by the highest fluorescence intensity of tumor sites. The fluorescence signals lasted even for 24 h after injection. Also, the ex vivo fluorescence intensity of tumors receiving IHM nanocatalysts was stronger than that from free IR820 groups (Fig. 8c and d). These results suggest the prominent ability of IHM nanocatalysts to promote their accumulation in tumor sites by the enhanced permeability and retention (EPR) effect combined with HA-mediated tumor targeting and to protect IR820 from degradation and body clearance. Furthermore, the ex vivo fluorescence signals of the livers of tumor-bearing mice treated with IHM nanocatalysts were appreciably higher than those of tumors and other organs due to the unavoidable capture of nanoparticles by the reticuloendothelial system. Similar biodistribution of MOF-based nanoparticles in tumor-bearing mice was observed elsewhere [16,17,55].

Based on the maximum accumulation of IHM nanocatalysts in 4 T1 tumor sites after 4 h post-injection (Fig. 8a), their photothermal performance on the tumor was evaluated by irradiating the tumor sites with 808 nm NIR laser ( $1.0 \text{ W/cm}^2$ ) and monitoring the change of tumor temperature. As revealed in Fig. 8e and f, a substantial rise in local tumor temperature was observed in the IHM nanocatalyst group. In contrast, the tumor temperature of free IR820-treated mice with NIR irradiation was only somewhat higher than that of the control group injected with the saline solution due to the poor tumor accumulation of IR820. Hyperthermia above  $50 \text{ }^\circ\text{C}$  has been demonstrated to induce irreversible damage to cancer cells [10,56]. According to the above results, through the fluorescence imaging guidance combined with NIR

laser irradiation, the IHMs effectively elevated tumor temperature, which is beneficial for enhanced phototherapy-mediated tumor treatment.

### 3.10. Inhibition of in vivo tumor growth and metastasis

Encouraged by the outstanding in vitro anticancer effects and sound tumor accumulation of IHM nanocatalysts, their capability of inhibiting in vivo tumor growth and metastasis was further studied with the 4 T1 tumor model in female BALB/c mice (Fig. 9a). As presented in Fig. 9b, compared to saline as the control group, the administration of IHM nanocatalysts without laser irradiation or free IR820 molecules with laser irradiation showed limited suppression of tumor growth during treatment. This signifies that the single nanocatalyst-based CDT or free IR820-mediated phototherapy could not arrest tumor growth effectively. In contrast, for the group treated with IHM nanocatalysts plus laser irradiation, the combination of phototherapy and CDT appreciably inhibited tumor growth during a 14-day evaluation period. Also, after 14-day treatment, visibly shrinking tumors were observed in 4 T1 tumor-bearing mice receiving IHM nanocatalysts and laser irradiation (Fig. S17). Corresponding to the in vivo tumor growth inhibition data, the weight and size of tumors collected from the euthanized mice treated with IHM nanocatalysts plus laser irradiation were the smallest among the mice receiving other treatments (Fig. 9c and d). In the H&E staining images of the tumor sections (Fig. 10a), the IHM nanocatalyst group with laser irradiation exhibited the largest necrotic and acellular area compared to other treatment groups. Also, this treatment led to the lowest level of cell proliferation by Ki67 staining (Fig. 10a and b). Additionally, the GPX4 staining images revealed that the tumor sections of mice receiving IHM nanocatalysts and laser irradiation showed a significant decrease in GPX4 expression compared to other treatment groups (Fig. 10a and c). This further demonstrates that the IHM nanocatalysts exposed to NIR laser irradiation can effectively deplete the GSH of tumor cells by  $\text{Fe}^{3+}$ -induced GSH oxidation and  $^1\text{O}_2/\cdot\text{OH}$ -involved

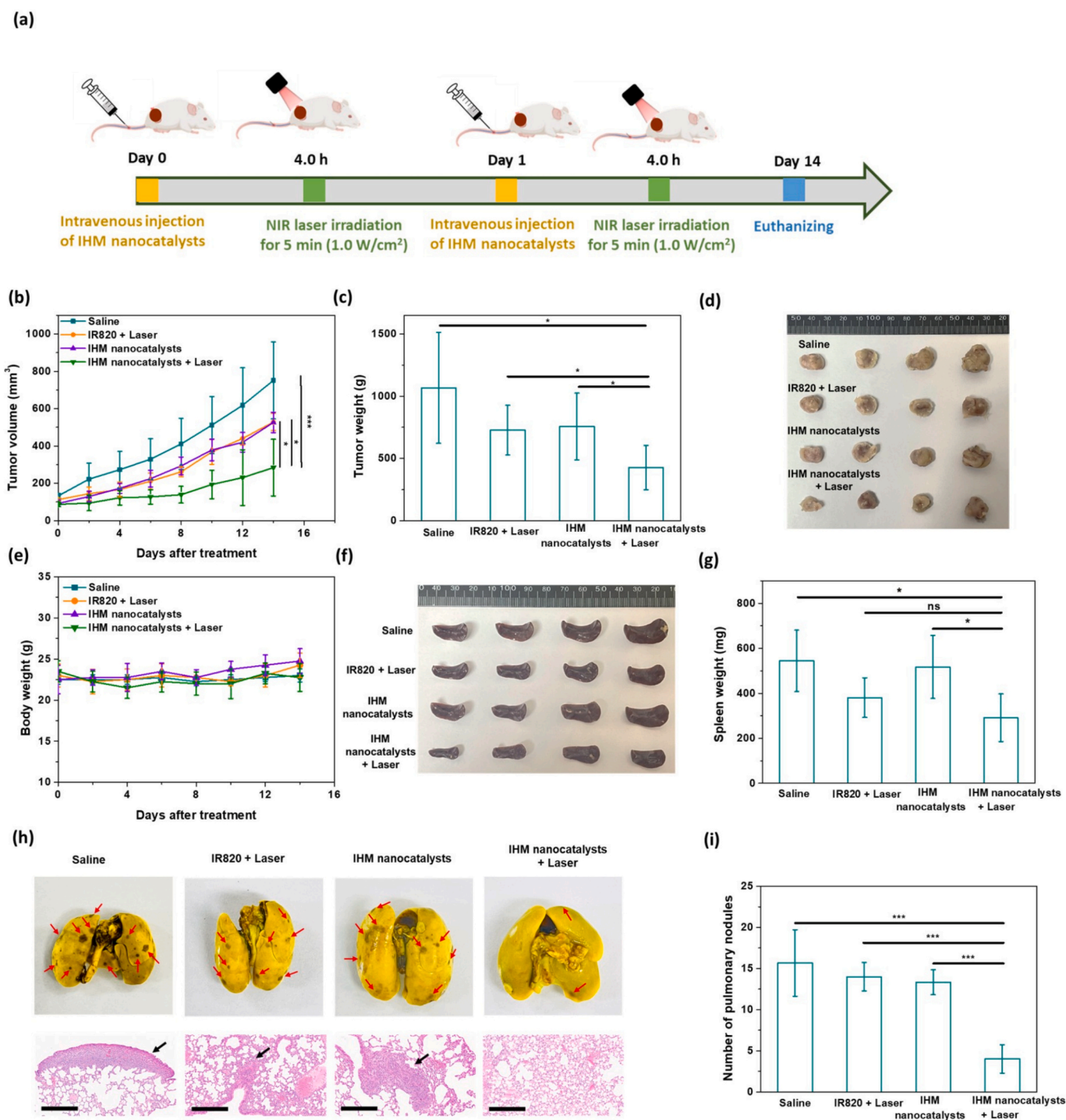


**Fig. 9.** (a) Schematic illumination of the in vivo antitumor study. (b) Tumor growth inhibition profiles of 4 T1 tumor-bearing mice receiving various treatments. (c) Weight and (d) photographs of the tumors collected from the euthanized mice on day 14 after treatment. (e) Body weight of 4 T1 tumor-bearing mice receiving various treatments. (f) Photographs and (g) weight of spleen harvested from the euthanized mice on day 14 after treatment. (h) Representative photographs of the lung tissues (top) and H&E staining of lung tissue sections (bottom) from 4 T1 tumor-bearing mice receiving various treatments. Red and black arrows indicate metastatic nodules and tumors, respectively. (i) Quantitative analysis of pulmonary metastatic nodules from Fig. 9h and S18. \* $p < 0.05$ , \*\* $p < 0.01$ , \*\*\* $p < 0.001$ , ns  $> 0.05$ . (For interpretation of the references to colour in this figure legend, the reader is referred to the web version of this article.)

GSH consumption, thereby causing GPX4 down-regulation. When the activity of GPX4 in cancer cells was inhibited, the capability of the tumor cells to scavenge ROS was remarkably diminished, thus enhancing ROS-mediated LPO to elicit ferroptosis. Based on the above results, it was concluded that the combined phototherapy and CDT of IHM nanocatalysts could execute potent antitumor effects by hyperthermia-induced cell death and ROS-mediated mitochondrial damage and

ferroptosis. Moreover, the treated mice in all groups exhibited nearly unchanged body weight over time, indicating that the formulations used in this study did not cause severe acute toxicity (Fig. 9e).

Recently, splenomegaly caused by leukemoid reactions is known to be a vital clinical symptom that is observed in the late stages of breast cancer [7,53,57]. As revealed in Fig. 9f and g, the spleens of mice receiving IHM nanocatalysts and laser irradiation have the smallest size

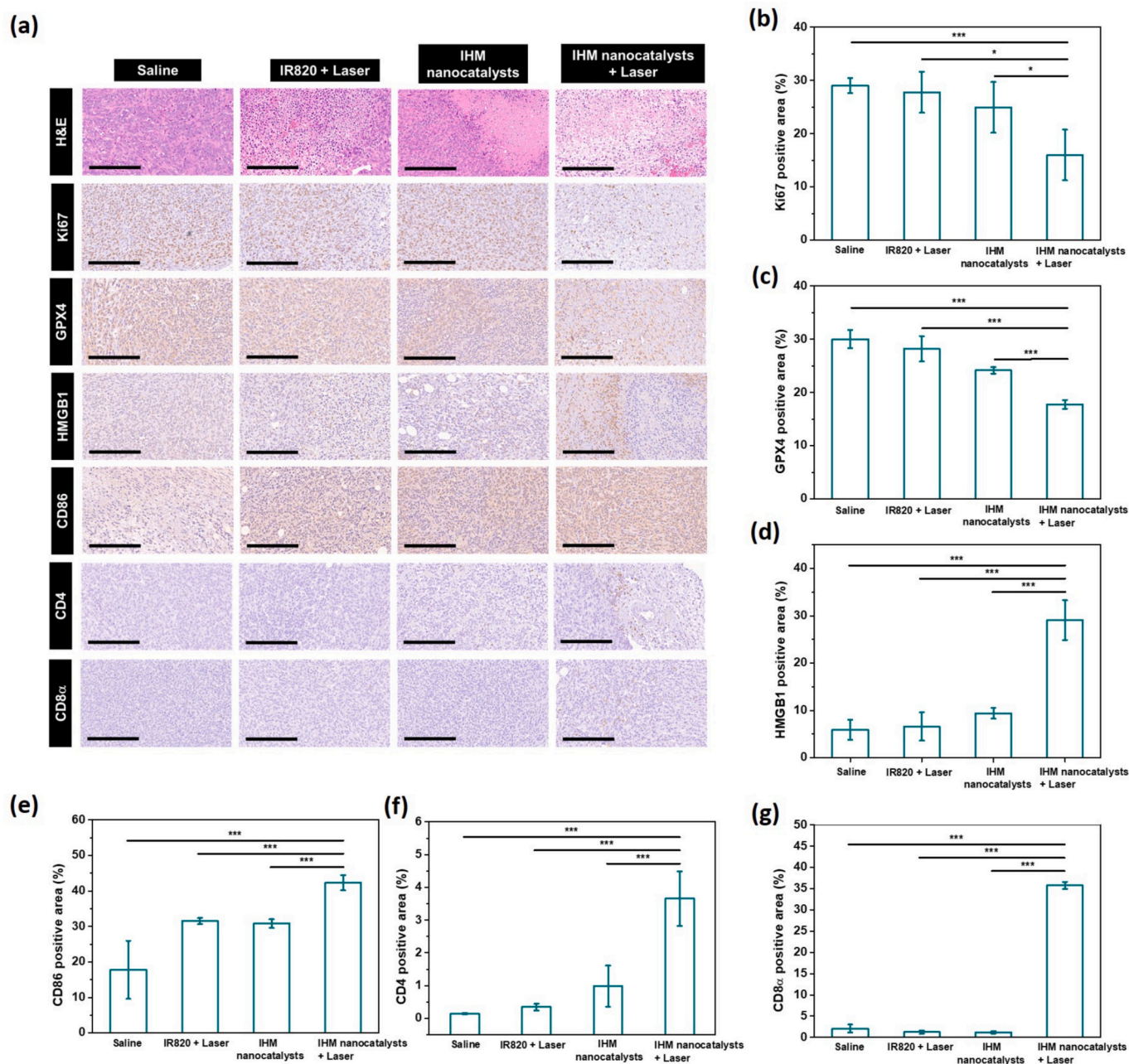


**Fig. 10.** (a) H&E, ki67, GPX4, HMGB1, CD86, CD4, and CD8α staining images of tumor sections from 4 T1 tumor-bearing receiving different treatments. Scale bars are 200 μm. Quantification of the positive percentage of (b) ki67, (c) GPX4, (d) HMGB1, (e) CD86, (f) CD4, and (g) CD8α cells according to Fig. 10a. \* $p < 0.05$ , \*\* $p < 0.01$ , \*\*\* $p < 0.001$ , ns  $> 0.05$ .

and lowest weight than mice with other treatments. This illustrates that the combined phototherapy and CDT delivered by IHM nanocatalysts could prominently reduce splenomegaly in treated mice by effectively inhibiting 4 T1 tumor growth. On the other hand, to evaluate the inhibitory effect of lung metastasis, the lung tissues were collected from 4 T1 tumor-bearing mice after the treatment and stained with Bouin's solution. As presented in Fig. 9h, i, and S18, the IHM nanocatalysts with laser irradiation group displayed the fewest metastatic nodules compared with other treatment groups. Also, the metastasis of 4 T1 cells to the liver was considerably decreased in the IHM nanocatalysts plus the laser irradiation group (Fig. S19). By contrast, for the single IR820-based phototherapy or IHM nanocatalyst-mediated CDT groups, significant metastasis of 4 T1 cells to the lung and liver was observed (Fig. 9h, i, S18, and S19). These findings suggest that the IHM nanocatalysts exposed to NIR laser irradiation effectively inhibited 4 T1 tumor growth

and metastasis by photo/chemodynamic therapy. Notably, no significant damage was observed in major organs of mice treated with IHM nanocatalysts and laser irradiation because the NIR irradiation as hyperthermia and ROS trigger was employed exclusively on tumors only (Fig. S19).

### 3.11. Enhanced antitumor immune response

Immunohistochemical staining of tumor sections was used to confirm whether the combined phototherapy and CDT of IHM nanocatalysts enhanced antitumor immune responses. As presented in Fig. 10a and d, the IHM nanocatalysts plus laser irradiation markedly promote the release of HMGB1 from the nuclei to the extracellular space compared to other treatments, consistent with cellular fluorescence images of HMGB1 staining (Fig. 7d). As mentioned in some previous

works [58–60], ICD stimulates the maturation of DCs to initiate anti-tumor immunity. Note that the CD86<sup>+</sup> mature DC level of the IHM nanocatalysts and laser irradiation group is appreciably higher than that of other treatment groups (Fig. 10a and e). This indicates that massive DAMPs generated by photo/chemodynamic therapy could attract receptors and ligands on DCs and activate immature DCs to transition to a mature phenotype. Moreover, CD4<sup>+</sup> and CD8 $\alpha$ <sup>+</sup> T cells inside tumors were appreciably increased after treatment of IHM nanocatalysts plus laser irradiation (Fig. 10a, f, and g). Several studies showed that CD4<sup>+</sup> T cells played a crucial role in regulating adaptive immunities, and CD8 $\alpha$ <sup>+</sup> T cells could hinder tumor growth and motivate cytotoxic T lymphocytes (CTLs) to eradicate tumor cells [58,59,61,62]. Based on these findings, it was concluded that the photo/chemodynamic therapy of IHM nanocatalysts facilitated ICD to promote the maturation of DCs, followed by the migration of mature DCs into tertiary lymphoid structures for activation and infiltration of CTLs (Scheme 1b). These activated T cells initiate antitumor immunity in response to the presence of tumors. Importantly, considering that the distant lung metastasis of the tumor did not receive light irradiation, the effective inhibition of lung metastasis in IHM nanocatalysts and laser irradiation group validates that the adaptive antitumor immunity activated by the combination of phototherapy and CDT could hinder cancer cells escape from the primary tumor.

#### 4. Conclusions

To inhibit breast tumor growth and metastasis by combining phototherapy, CDT, and enhanced immune response, we developed the CD44-targeting IHM nanocatalysts using a DMF-free and mild approach. The IHM nanocatalysts exhibited a spindle-like shape, high IR820 payloads (ca 19.1 wt%), sound colloidal stability, and enhanced photothermal effect and stability of IR820. The GSH-triggered disintegration of IHM nanocatalysts in a weakly acidic milieu remarkably accelerated Fe<sup>3+</sup> and IR820 release. Notably, the IHM nanocatalysts not only produced Fe<sup>2+</sup> by GSH-induced Fe<sup>3+</sup> reduction, but also displayed thermo/acidity-enhanced Fe<sup>3+</sup>-mediated Fenton reaction, thereby boosting conversion of H<sub>2</sub>O<sub>2</sub> into  $\cdot$ OH. Through CD44-mediated endocytosis, the IHM nanocatalysts internalized by 4 T1 cells under NIR laser irradiation considerably depleted intracellular GSH and generated massive  $\cdot$ OH and <sup>1</sup>O<sub>2</sub>, thus leading to apoptosis and ferroptosis via mitochondria damage and LPO, and promoting ICD to release CRT and HMGB1. After being accumulated in the tumor, the IHM nanocatalysts effectively inhibited tumor growth and lung metastasis by imaging-guided phototherapy and CDT with the assistance of enhanced antitumor immune response initiated by ICD-triggered maturation of DCs and activation of CTLs. These results demonstrate that the IHM nanocatalysts show great promise in inhibiting tumor growth and metastasis by combined anti-tumor therapy.

#### CRedit authorship contribution statement

**Tzu-Chen Lin:** Validation, Methodology, Investigation, Formal analysis, Conceptualization. **I-Ju Liu:** Validation, Resources, Investigation. **Hsiang-Yun Chih:** Resources, Investigation, Formal analysis. **Bor-Show Tzang:** Resources, Methodology, Investigation. **Ju-An Liang:** Visualization, Resources, Methodology, Investigation. **Chia-Wei Kuo:** Methodology, Investigation. **Chun-Yu Hung:** Resources, Investigation. **Tsai-Ching Hsu:** Writing – review & editing, Supervision, Resources, Investigation, Funding acquisition. **Wen-Hsuan Chiang:** Writing – review & editing, Writing – original draft, Supervision, Project administration, Investigation, Funding acquisition, Conceptualization.

#### Declaration of competing interest

The authors declare that they have no known competing financial interests or personal relationships that could have appeared to influence

the work reported in this paper.

#### Acknowledgments

This work is supported by the National Science and Technology Council (NSTC 113-2628-E-005-002-MY3 and NSTC 113-2622-E-005-017), National Chung Hsing University and Chung Shan Medical University (NCHU-CSMU 11301), Taiwan.

#### Appendix A. Supplementary data

Supplementary data to this article can be found online at <https://doi.org/10.1016/j.ijbiomac.2025.142975>.

#### Data availability

Data will be made available on request.

#### References

- [1] Z.W. Yang, L.W. Wang, J. Zhang, J. Liu, X. Yu, Application of bismuth sulfide based nanomaterials in cancer diagnosis and treatment, *Nano Today* 49 (2023) 101799.
- [2] J. Lu, Y. Yang, Q. Xu, Y. Lin, S. Feng, Y. Mao, D. Wang, S. Wang, Q. Zhao, Recent advances in multi-configurable nanomaterials for improved chemodynamic therapy, *Coord. Chem. Rev.* 274 (2023) 214861.
- [3] W. Li, J. Zhou, Y. Zhang, S. Liu, R. Li, S. Gai, H. Ding, L. Zhong, P. Yang, A collective hyperthermia-facilitated glutathione inhibition strategy for boosted oxidative stress treatment, *Chem. Eng. J.* 485 (2024) 150056.
- [4] T. Liu, M. Zhu, X. Chang, X. Tang, P. Yuan, R. Tian, Z. Zhu, Y. Zhang, X. Chen, Tumor-specific photothermal-therapy-assisted immunomodulation via multiresponsive adjuvant nanoparticles, *Adv. Mater.* 35 (2023) e2300086.
- [5] S. Zhang, J. Wang, Z. Kong, X. Sun, Z. He, B. Sun, C. Luo, J. Sun, Emerging photodynamic nanotherapeutics for inducing immunogenic cell death and potentiating cancer immunotherapy, *Biomaterials* 282 (2022) 121433.
- [6] M.U. Farooq, C.H. Lawrie, N.N. Deng, Engineering nanoparticles for cancer immunotherapy: current achievements, key considerations and future perspectives, *Chem. Eng. J.* 486 (2024) 150356.
- [7] N. Xu, A. Hu, X. Pu, J. Li, X. Wang, J. Wang, Z. Huang, X. Liao, G. Yin, Fe(III)-chelated polydopamine nanoparticles for synergistic tumor therapies of enhanced photothermal ablation and antitumor immune activation, *ACS Appl. Mater. Interfaces* 14 (2022) 15894–15910.
- [8] W. Shao, Y. Yang, W. Shen, L. Ren, W. Wang, P. Zhu, Hyaluronic acid-conjugated methotrexate and 5-fluorouracil for targeted drug delivery, *Int. J. Biol. Macromol.* 273 (2024) 132671.
- [9] B. Ji, M. Wei, B. Yang, Recent advances in nanomedicines for photodynamic therapy (PDT)-driven cancer immunotherapy, *Theranostics* 12 (2022) 434–458.
- [10] Y.H. Chen, I.J. Liu, T.C. Lin, M.C. Tsai, S.H. Hu, T.C. Hsu, Y.T. Wu, B.S. Tzang, W. H. Chiang, PEGylated chitosan-coated nanophotosensitizers for effective cancer treatment by photothermal-photodynamic therapy combined with glutathione depletion, *Int. J. Biol. Macromol.* 266 (2024) 131359.
- [11] G. Zhang, X. Jiang, Y. Xia, P. Qi, J. Li, L. Wang, Z. Wang, X. Tian, Hyaluronic acid-conjugated lipid nanocarriers in advancing cancer therapy: a review, *Int. J. Biol. Macromol.* 299 (2025) 140146.
- [12] M. Su, Y. Zhang, L. Yang, H. Li, X. Li, J. Feng, L. Jia, Z. Zhang, Camptothecin-loaded and IR780-doped polydopamine nanomedicine used for multifunctional chemo-photothermal-photodynamic therapy for lung cancer, *J. Drug Deliv. Technol.* 97 (2024) 105657.
- [13] G.R. Nirmal, Z.C. Lin, C.H. Lin, C.T. Sung, C.C. Liao, J.Y. Fang, Polydopamine/IR820 nanoparticles as topical phototheranostics for inhibiting psoriasisform lesions through dual photothermal and photodynamic treatments, *Biomater. Sci.* 10 (2022) 6172–6189.
- [14] Y.L. Liu, T.H. Wang, N.T. Yeh, W.J. Huang, B.S. Tzang, I.T. Wu, H.Y. Chin, S.H. Hu, T.C. Hsu, W.H. Chiang, Tumor-activated targetable photothermal chemotherapy using IR780/zoledronic acid-containing hybrid polymeric nanoassemblies with folate modification to treat aggressive breast cancer, *Nanoscale* 16 (2024) 1415–1427.
- [15] J. Chen, Y. Wang, H. Niu, Y. Wang, A. Wu, C. Shu, Y. Zhu, Y. Bian, K. Lin, Metal-organic framework-based nanoagents for effective tumor therapy by dual dynamics-amplified oxidative stress, *ACS Appl. Mater. Interfaces* 13 (2021) 45201–45213.
- [16] K.A. Liang, H.Y. Chih, I.J. Liu, N.T. Yeh, T.C. Hsu, H.Y. Chin, B.S. Tzang, W. H. Chiang, Tumor-targeted delivery of hyaluronic acid/polydopamine-coated Fe<sup>2+</sup>-doped nano-scaled metal-organic frameworks with doxorubicin payload for glutathione depletion-amplified chemodynamic-chemo cancer therapy, *J. Colloid Interface Sci.* 677 (2025) 400–415.
- [17] H. Deng, J. Zhang, Y. Yang, J. Yang, Y. Wei, S. Ma, Q. Shen, Chemodynamic and photothermal combination therapy based on dual-modified metal-organic framework for inducing tumor ferroptosis/pyroptosis, *ACS Appl. Mater. Interfaces* 14 (2022) 24089–24101.

- [18] B. Liu, Y. Bian, S. Liang, M. Yuan, S. Dong, F. He, S. Gai, P. Yang, Z. Cheng, J. Lin, One-step integration of tumor microenvironment-responsive calcium and copper peroxides nanocomposite for enhanced chemodynamic/ion-interference therapy, *ACS Nano* 16 (2022) 617.
- [19] Z. Liu, S. Liu, B. Liu, Y. Bian, M. Yuan, C. Yang, Q. Meng, C. Chen, P. Ma, J. Lin, Fe(III)-naphthazarin metal-phenolic networks for glutathione-depleting enhanced ferroptosis-apoptosis combined cancer therapy, *Small* 19 (2023) 2207825.
- [20] F. Liu, S. Gong, M. Shen, T. He, X. Liang, Y. Shu, X. Wang, S. Ma, X. Li, M. Zhang, Q. Wu, C. Gong, A glutathione-activatable nanoplatfor for enhanced photodynamic therapy with simultaneous hypoxia relief and glutathione depletion, *Chem. Eng. J.* 403 (2021) 126305.
- [21] Z. Xie, S. Liang, X. Cai, B. Ding, S. Huang, Z. Hou, P. Ma, Z. Cheng, J. Lin, O<sub>2</sub>-cu/ZIF-8@Ce6/ZIF-8@F127 composite as a tumor microenvironment-responsive nanoplatfor with enhanced photo-/chemodynamic antitumor efficacy, *ACS Appl. Mater. Interfaces* 11 (2019) 31671–31680.
- [22] Z. Zhao, W. Wang, C. Li, Y. Zhang, T. Yu, R. Wu, J. Zhao, Z. Liu, J. Liu, H. Yu, Reactive oxygen species-activatable liposomes regulating hypoxic tumor microenvironment for synergistic photo/chemodynamic therapies, *Adv. Funct. Mater.* 29 (2019) 1905013.
- [23] B. Wang, Y. Dai, Y. Kong, W. Du, H. Ni, H. Zhao, Z. Sun, Q. Shen, M. Li, Q. Fan, Tumor microenvironment-responsive Fe(III)-porphyrin nanotheranostics for tumor imaging and targeted chemodynamic-photodynamic therapy, *ACS Appl. Mater. Interfaces* 12 (2020) 53634–53645.
- [24] Y. Wang, J. Chen, Z. Tian, M. Zhu, Y. Zhu, Potassium ferrate-loaded porphyrin-based (VI) metal-organic frameworks for combined photodynamic and chemodynamic tumor therapy, *J. Inorg. Mater.* 36 (2021) 157.
- [25] X. Deng, Z. Shao, Y. Zhao, Solutions to the drawbacks of photothermal and photodynamic cancer therapy, *Adv. Sci.* 8 (2021) 2002504.
- [26] Z. Xie, T. Fan, J. An, W. Choi, Y. Duo, Y. Ge, B. Zhang, G. Nie, N. Xie, T. Zheng, Y. Chen, H. Zhang, J.S. Kim, Emerging combination strategies with phototherapy in cancer nanomedicine, *Chem. Soc. Rev.* 49 (2020) 8065–8087.
- [27] W. Zuo, N. Liu, Z. Chang, J. Liu, Q. Jin, L. Chen, X. Zhu, Single-site bimetallic nanosheet for imaging guided mutually-reinforced photothermal-chemodynamic therapy, *Chem. Eng. J.* 442 (2022) 136125.
- [28] P. Manivasagan, A. Joe, H.W. Han, T. Thambi, M. Selvaraj, K. Chidambaram, J. Kim, E.S. Jang, Recent advances in multifunctional nanomaterials for photothermal-enhanced Fenton-based chemodynamic tumor therapy, *Mater. Today Bio.* 13 (2022) 100197.
- [29] T.H. Wang, M.Y. Shen, N.T. Yeh, Y.H. Chen, T.C. Hsu, H.Y. Chin, Y.T. Wu, B. S. Tzang, W.H. Chiang, Photothermal nanozymes to self-augment combination cancer therapy by dual-glutathione depletion and hyperthermia/acidity-activated hydroxyl radical generation, *J. Colloid Interface Sci.* 650 (2023) 1698–1714.
- [30] E.E. Sweeney, J. Cano-Mejia, R. Fernandes, Photothermal therapy generates a thermal window of immunogenic cell death in neuroblastoma, *Small* 14 (2018) 1800678.
- [31] H. Hao, M. Yu, Y. Yi, S. Sun, X. Huang, C. Huang, Y. Liu, W. Huang, J. Wang, J. Zhao, M. Wu, Mesoporous calcium peroxide-ignited NO generation for amplifying photothermal immunotherapy of breast cancer, *Chem. Eng. J.* 437 (2022) 135371.
- [32] D. Zhang, J. Zhang, Q. Li, A. Song, Z. Li, Y. Luan, Cold to hot: rational design of a minimalist multifunctional photo-immunotherapy nanoplatfor toward boosting immunotherapy capability, *ACS Appl. Mater. Interfaces* 11 (2019) 32633–32646.
- [33] S. Xiao, Y. Lu, M. Feng, M. Dong, Z. Cao, X. Zhang, Y. Chen, J. Liu, Multifunctional FeS<sub>2</sub> theranostic nanoparticles for photothermal-enhanced chemodynamic/photodynamic cancer therapy and photoacoustic imaging, *Chem. Eng. J.* 396 (2020) 125294.
- [34] Y. Chen, P. Liu, C. Zhou, T. Zhang, T. Zhou, D. Men, G. Jiang, L. Hang, Gold nanopyramid@copper sulfide nanotheranostics for image-guided NIR-II photo/chemodynamic cancer therapy with enhanced immune response, *Acta Biomater.* 158 (2023) 649–659.
- [35] X. Wan, H. Zhong, W. Pan, Y. Li, Y. Chen, N. Li, B. Tang, Programmed release of dihydroartemisinin for synergistic cancer therapy using a CaCO<sub>3</sub> mineralized metal-organic framework, *Angew. Chem. Int. Ed. Engl.* 58 (2019) 14134–14139.
- [36] F. Liu, L. Lin, Y. Zhang, Y. Wang, S. Sheng, C. Xu, H. Tian, X. Chen, A tumor-microenvironment-activated nanozyme-mediated theranostic nanoreactor for imaging-guided combined tumor therapy, *Adv. Mater.* 31 (2019) 1902885.
- [37] X.X. Yang, X. Xu, M.F. Wang, H.Z. Xu, X.C. Peng, N. Han, T.T. Yu, L.G. Li, Q.R. Li, X. Chen, Y. Wen, T.F. Li, A nanoreactor boosts chemodynamic therapy and ferroptosis for synergistic cancer therapy using molecular amplifier dihydroartemisinin, *J. Nanobiotechnology* 20 (2022) 230.
- [38] C.H. Yu, A.C. Sun, C.W.K. Wu, M.T. Gao, C. Wu, H.M.D. Wang, Monacolin-K loaded MIL-100(Fe) metal-organic framework induces ferroptosis on metastatic triple-negative breast cancer, *Chem. Eng. J.* 498 (2024) 154751.
- [39] L. Bai, E. Shi, Y. Li, M. Yang, C. Li, C. Li, Y. Wang, Y. Wang, Oxyhemoglobin-based nanophotosensitizer for specific and synergistic photothermal and photodynamic therapies against porphyromonas gingivalis oral infection, *ACS Biomater. Sci. Eng.* 9 (2023) 485–497.
- [40] D. Zhang, J. Zhang, Q. Li, H. Tian, N. Zhang, Z. Li, Y. Luan, pH- and enzyme-sensitive IR820-paclitaxel conjugate self-assembled nanovehicles for near-infrared fluorescence imaging-guided chemo-photothermal therapy, *ACS Appl. Mater. Interfaces* 10 (2018) 30092–30102.
- [41] H. Fan, S. Chen, Z. Du, T. Yan, G. Alimu, L. Zhu, R. Ma, N. Alifu, X. Zhang, New indocyanine green therapeutic fluorescence nanoplates assisted high-efficient photothermal therapy for cervical cancer, *Dyes Pigments* 200 (2022) 110174.
- [42] C. Qiao, R. Zhang, Y. Wang, Q. Jia, X. Wang, Z. Yang, T. Xue, R. Ji, X. Cui, Z. Wang, Rabies virus-inspired metal-organic frameworks (MOFs) for targeted imaging and chemotherapy of glioma, *Angew. Chem. Int. Ed. Engl.* 59 (2020) 16982–16988.
- [43] T. Yan, G. Alimu, L. Zhu, H. Fan, L. Zhang, Z. Du, R. Ma, S. Chen, N. Alifu, X. Zhang, PpIX/IR-820 dual-modal therapeutic agents for enhanced PDT/PTT synergistic therapy in cervical cancer, *ACS Omega* 7 (2022) 44643–44656.
- [44] B. Qu, X. Zhang, Y. Han, X. Peng, J. Sun, R. Zhang, IR820 functionalized melanin nanoplates for dual-modal imaging and photothermal tumor eradication, *Nanoscale Adv.* 2 (2020) 2587–2594.
- [45] J. Xiao, L. Hai, Y. Li, H. Li, M. Gong, Z. Wang, Z. Tang, L. Deng, D. He, An ultrasmall Fe<sub>3</sub>O<sub>4</sub>-decorated polydopamine hybrid nanozyme enables continuous conversion of oxygen into toxic hydroxyl radical via GSH-depleted cascade redox reactions for intensive wound disinfection, *Small* 18 (2022) 2105465.
- [46] L.S. Lin, J. Song, L. Song, K. Ke, Y. Liu, Z. Zhou, Z. Shen, J. Li, Z. Yang, W. Tang, G. Niu, H.H. Yang, X. Chen, Simultaneous Fenton-like ion delivery and glutathione depletion by MnO<sub>2</sub>-based nanoagent to enhance chemodynamic therapy, *Angew. Chem. Int. Ed. Engl.* 57 (2018) 4902–4906.
- [47] W. Chen, J. Liu, C. Zheng, Q. Bai, Q. Gao, Y. Zhang, K. Dong, T. Lu, Research progress on improving the efficiency of CDT by exacerbating tumor acidification, *Int. J. Nanomedicine* 17 (2022) 2611–2628.
- [48] J. Zhuang, B. Wang, H. Chen, K. Zhang, N. Li, N. Zhao, B.Z. Tang, Efficient NIR-II type-I AIE photosensitizer for mitochondria-targeted photodynamic therapy through synergistic apoptosis-ferroptosis, *ACS Nano* 17 (2023) 9110–9125.
- [49] L. Ke, F. Wei, L. Xie, J. Karges, Y. Chen, L. Ji, H. Chao, A biodegradable iridium(III) coordination polymer for enhanced two-photon photodynamic therapy using an apoptosis-ferroptosis hybrid pathway, *Angew. Chem. Int. Ed. Engl.* 61 (2022) e202205429.
- [50] T. Liu, W. Liu, M. Zhang, W. Yu, F. Gao, C. Li, S.B. Wang, J. Feng, X.Z. Zhang, Ferrous-supply-regeneration nanoengineering for cancer-cell-specific ferroptosis in combination with imaging-guided photodynamic therapy, *ACS Nano* 12 (2018) 12181–12192.
- [51] X. Zhang, Y. Lu, D. Jia, W. Qiu, X. Ma, X. Zhang, Z. Xu, F. Wen, Acidic microenvironment responsive polymeric MOF-based nanoparticles induce immunogenic cell death for combined cancer therapy, *J. Nanobiotechnology* 19 (2021) 455.
- [52] Z. Feng, G. Chen, M. Zhong, L. Lin, Z. Mai, Y. Tang, G. Chen, W. Ma, G. Li, Y. Yang, Z. Yu, M. Yu, An acid-responsive MOF nanomedicine for augmented anti-tumor immunotherapy via a metal ion interference-mediated pyroptotic pathway, *Biomaterials* 302 (2023) 122333.
- [53] G. Yang, L. Xu, Y. Chao, J. Xu, X. Sun, Y. Wu, R. Peng, Z. Liu, Hollow MnO<sub>2</sub> as a tumor-microenvironment-responsive biodegradable nano-platfor for combination therapy favoring antitumor immune responses, *Nat. Commun.* 8 (2017) 902.
- [54] E. Panzarini, V. Inguscio, L. Dini, Immunogenic cell death: can it be exploited in photodynamic therapy for cancer? *Biomed. Res. Int.* 2013 (2013) 482160.
- [55] N.T. Yeh, T.C. Lin, I.J. Liu, S.H. Hu, T.C. Hsu, H.Y. Chin, B.S. Tzang, W.H. Chiang, Hyaluronic acid-covered ferric ion-rich nanobullets with high zoledronic acid payload for breast tumor-targeted chemo/chemodynamic therapy, *Int. J. Biol. Macromol.* 279 (2024) 135271.
- [56] M.H. Hsieh, T.H. Wang, S.H. Hu, T.C. Hsu, J.L. Yow, B.S. Tzang, W.H. Chiang, Tumor site-specific PEG detachment and active tumor homing of therapeutic PEGylated chitosan/folate-decorated polydopamine nanoparticles to augment antitumor efficacy of photothermal/chemo combination therapy, *Chem. Eng. J.* 446 (2022) 137243.
- [57] M. Liu, X. Jin, X. He, L. Pan, X. Zhang, Y. Zhao, Macrophages support splenic erythropoiesis in 4T1 tumor-bearing mice, *PLoS One* 10 (2015) e0121921.
- [58] W. Ni, J. Wu, H. Fang, Y. Feng, Y. Hu, L. Lin, J. Chen, F. Chen, H. Tian, Photothermal-chemotherapy enhancing tumor immunotherapy by multifunctional metal-organic framework based drug delivery system, *Nano Lett.* 21 (2021) 7796–7805.
- [59] K. Sun, J. Yu, J. Hu, W. Yang, X. Chu, L. Chen, X. Deng, B. Sun, Z. Wang, Photothermal enhanced polyphenol-based nanofibers ameliorate catalytic efficiency of ferroptosis for synergistic tumor therapy, *Chem. Eng. J.* 470 (2023) 144360.
- [60] Z. Xiao, R. Wang, X. Wang, H. Yang, J. Dong, X. He, Y. Yang, J. Guo, J. Cui, Z. Zhou, Impaired function of dendritic cells within the tumor microenvironment, *Front. Immunol.* 14 (2023) 1213629.
- [61] L. Xie, J. Li, G. Wang, W. Sang, M. Xu, W. Li, J. Yan, B. Li, Z. Zhang, Q. Zhao, Z. Yuan, Q. Fan, Y. Dai, Phototheranostic metal-phenolic networks with antiexosomal PD-L1 enhanced ferroptosis for synergistic immunotherapy, *J. Am. Chem. Soc.* 144 (2022) 787–797.
- [62] Y.P. Jia, K. Shi, F. Yang, J.F. Liao, R.X. Han, L.P. Yuan, Y. Hao, M. Pan, Y. Xiao, Z. Y. Qian, X.W. Wei, Multifunctional nanoparticle loaded injectable thermoresponsive hydrogel as NIR controlled release platfor for local photothermal immunotherapy to prevent breast cancer postoperative recurrence and metastases, *Adv. Funct. Mater.* 30 (2020) 2001059.